UNIVERSITY OF CALIFORNIA
RIVERSIDE

Electronic and Magneto-Electronic Properties of Nanopatterned and Multilayered Graphene

A Dissertation submitted in partial satisfaction
of the requirements for the degree of

Doctor of Philosophy

in

Electrical Engineering

by

Sonia Ahsan

December 2013

Dissertation Committee:
Dr. Roger K. Lake, Chairperson
Dr. Alexander A. Balandin
Dr. Elaine D. Haberer

The Dissertation of Sonia Ahsan is approved:

Committee Chairperson

University of California, Riverside

Acknowledgments

I would first like to thank my advisor Prof. Roger Lake for his continuous guidance and encouragement in the course of my research. He has helped me grow professionally and has given me proper exposure to the academic and industrial research work in my field. He gave me freedom and opportunities to work on challenging research problems which helped me develop my original research ideas. His interactive guidance, high research standards and work ethics have been invaluable for the project. The distinguished lessons and experiences he has equipped me with will always stay with me throughout my future journey.

I would also thank Prof. Elaine D. Haberer and Prof. Alexander Balandin for taking the time to serve in my dissertation committee. I also thank them for numerous beneficial discussions that I had with them all along.

This work was supported in part by FAME, one of six centers of STARnet, a Semiconductor Research Corporation program sponsored by MARCO and DARPA.

I would like to thank Dr. Srinath Krisnan and Dr. Jia Feng for guiding me during my internship at GlobalFoundries. I greatly benefited from the internship on device integration.

I would also like to thank all the present and past group members for generating a research-friendly environment at LATTE. A special thanks to Dr. Masum Habib, Somaiya Sylvia for making my days at LATTE pleasant and memorable. My times

were also made memorable by all my friends and people at UC Riverside. I wish them all the best in life.

I would like to thank my parents, sisters, brother and in-laws for their continuous support. My parents have created the pedestal for me to stand here today. They have been my inspiration and guiding star. It would be impossible for me to accomplish this mission without the unconditional support and encouragement of my dearest and loving husband, Farhan Shahil. My little angel, Farisha S Shahil gave me the strength to reach the end of this journey. This work would not have been possible without the steadfast support and encouragement of them. This dissertation is dedicated to them.

On top of everything, all praise goes to the Almighty Allah; the most Gracious, the most merciful for blessing me with all good things I have and showing me the enlightened path.

The text of this dissertation, in part or in full, is a reprint of the material as it appears in the following journals and/or proceedings:

- Journal of applied Physics [1]. Reprinted with permission from [1]. © [2013] American Institute of Physics.

- Journal of applied Physics [2]. Reprinted with permission from [2]. © [2013] American Institute of Physics.

To my parents, husband and my daughter

ABSTRACT OF THE DISSERTATION

Electronic and Magneto-Electronic Properties of Nanopatterned and Multilayered Graphene

by

Sonia Ahsan

Doctor of Philosophy, Graduate Program in Electrical Engineering
University of California, Riverside, December 2013
Dr. Roger Lake, Chairperson

Various approaches to induce a band gap in graphene based structures are theoretically investigated. The band structure and the electron transport of the proposed devices are calculated using semi-empirical extended Huckel theory (EHT) coupled with the nonequilibrium Green's function (NEGF) formalism. We consider a stacked structure of two arm-chair nanoribbons and observe negative differential resistance (NDR) behavior in the simulated current-voltage ($I-V$) characteristics. The magnitude of the NDR decreases with an increase of the ribbon width. A 2D nanomesh structure of graphene patterned with a periodic array of nano holes is also investigated. The results suggest that the bandgap opening is a result of quantum confinement. However obtaining a modest bandgap in graphene often comes at the expense of strongly degraded electron mobility with lithographic difficulties. Therefore, an unconventional biasing approach of modulating the $I-V$ characteristics without inducing any bandgap is studied. In such a scheme, NDR is observed in both single layer and bi-layer graphene field-effect transistors. The NDR is an intrinsic property of graphene resulting from its symmetric band structure.

Experimentally, multiple layers of graphene tend to be misoriented with respect to each other. The effects of magnetic field and interlayer bias on the interlayer electron transport of large misoriented bilayer graphene nanoribbons is calculated. Edge states can result in a large peak in the transmission at the charge neutrality point that is several orders of magnitude larger than the surrounding low-energy transmission. The transmission is consistently asymmetric around the charge neutrality point for all structures with the value differing by up to 3 orders of magnitude within 50 meV on either side of the charge neutrality point. The low-energy states exhibit a high magnetoconductance ratio, and the magnetoconductance ratio tends to increase as the width of the ribbons decrease. The maximum value of magnetoconductance ratio for the 35 nm wide bilayer ribbons at 10T is 15,000%. The effect of the bias on the transmission gives rise to non-linear $I - V$ characteristics.

Contents

List of Tables

List of Figures

Chapter 1

Introduction

1.1 Background and Motivation

Over the past 50 years, down scaling of the silicon complementary metal-oxide-semiconductor (CMOS) technology provided increasing performance of computer chips and enabled progress in information technologies. However, as the electronic industry is working on the sub 10-nm technology node, it is widely expected that the downscaling of Si CMOS technology will not last much beyond 2020 [4] (see Fig.1.1). The problem of heat dissipation and the physical limitations of silicon are expected to end the era of silicon computer chips which enabled progress in information technologies. This fact motivates a search for alternative materials and computational paradigms that can, if not replace Si CMOS, then complement it in special-task information processing [5].

Carbon based electronics is one of the potential alternatives for low-power post CMOS applications. Carbon based electronics has been under investigation since the discovery of carbon nanotubes (CNT) [6]. CNTs demonstrated nearly ideal switching characteristics, increased device speed, and lower power consumption than traditional

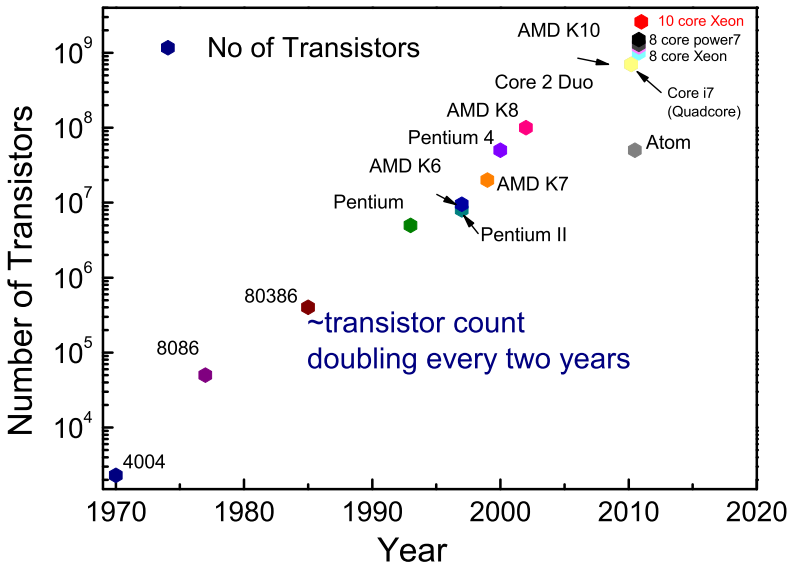

Figure 1.1: Scaling trend showing number of transistors on a chip between the years 1970 and 2011. Data is from publications by AMD and Intel Corporation

CMOS logic by utilizing band-to-band tunneling [7]. However, a manufacturable process is problematic due to the difficulty of sorting metallic CNTs from the semiconducting ones.

Another carbon allotrope, graphene [8, 9], has become one of the highly studied alternative materials for promising future device applications [10–13]. Several interesting properties make this material attractive for device applications. It is flat 2D system entirely composed of surface atoms and can be obtained with a low defect density (1 in 10^8) [14]. Many interesting physical phenomena can be observed in this near defect free material. The charge carriers, which can be tuned between electrons and holes, are massless, relativistic-like particles which exhibit the quantum Hall effect (integer and fractional) in magnetic fields [15–19]. They have very high mobility over a broad temperature range and one of the highest at room temperature (RT) [20]. Graphene has negligible spin orbit coupling which allows spin polarization to survive

over micrometer distances. Furthermore, it is also one of the strongest [21] materials ever measured and also possesses very high thermal conductivity [22]. All these outstanding properties of graphene can be utilized in a wide range of applications from computing displays and optoelectronics to composite materials.

Although graphene has these many unique properties beneficial for electronics, lack of bandgap presents a serious hurdle for its applications in digital logic circuits. A large number of research groups have attempted to solve this problem via application of an electric field [23], quantum confinement of carriers in nanometer-scale ribbons [24], surface functionalization with various atoms [25], and strain engineering [26]. A more effective way to modify the band structure of graphene is to stack two monolayers to form a bilayer which has a zero band-gap electronic structure [27, 28]. One unique property of bilayer graphene is that the bandgap can be tuned from 0 eV to about 0.25 eV by an applied vertical field [29, 30]. The outcome of all these efforts are a modest band gap opening of few-hundred meV, which often comes at the expense of a strongly degraded electron mobility. Practical applications of graphene in digital circuits require a band-gap on the order of 1 eV at room temperature. The performance of a field effect transistor (FET) using bilayer graphene as the channel material was studied [31]. It was shown that this FET has a poor I_{on}/I_{off} ratio due to strong band-to-band tunneling. FET utizing tunneling properties (i.e., TFET) using bilayer graphene layer showed on/off ratio of 10^3 [32].

Various garphene based FETs have been proposed utilizing different properties such as interlayer distance modulation [33], $p-n$ junctions [34], $p-n-p$ junctions [35] and bilayer exciton condensate [36] etc. Negative differential resistance (NDR) was predicted to occur in devices based on a single-gated graphene sheet [37], chemical doping in a GNR [38], and a strained GNR [39]. Do et al. [37] reported that NDR can be observed in $p^+ - p$ junctions of zigzag GNRs created by field-effect doping.

Recently, a strong NDR behavior was also predicted in a $p-n$ junction of single layer chemically or electrically doped graphene [40]. However, many of these FET and NDR type devices have relatively complex architectures [40–42], limited scalability [43], or low on-off or peak-to-valley current ratios [37, 38].

One remarkable property of graphene is that when graphene layers are stacked together, as is often the case in chemical vapor deposition (CVD) and multilayer epitaxial graphene [44, 45], the layers tend to be rotated (i.e., twisted, misoriented) with respect to each other at certain angles corresponding to allowed growth orientations with respect to the substrate [45–47]. Bi-layer graphene with a relative rotation between the layers is known as misoriented or twisted bilayer graphene. The misoriented structures [46–50] can be obtained by different experimental methods such as mechanical exfoliation [51], segregation of graphene on Ni film [52], and unzipping of a carbon nanotube [53]. The electronic structure of misoriented bilayer graphene is highly sensitive to the stacking geometry [15, 16]. Several theoretical calculations for such misoriented structures have been carried out using various methodologies such as density functional theory [46, 48–50], empirical tight binding [54], and continuum models [55]. Both the theoretical and experimental studies [47] showed that in misoriented bilayer graphene with twist angles greater than $\sim 3^\circ$, the low-energy carriers behave as massless Dirac Fermions with a reduced Fermi velocity similar to that of single layer graphene. With a twist angle greater than $\sim 10^\circ$, the layers are effectively decoupled and act as independent layers. In order to investigate the electronic properties, it is necessary to analyze the interlayer coherent transmission ($T(E)$) of these decoupled misoriented layers. Moreover $T(E)$ is a strong function of the twist angle, and it can be strongly suppressed giving high interlayer contact resistances [56]. This electronic decoupling and high interlayer resistance is a coherent quantum effect resulting from destructive interference between the electron wavefunctions of the

two rotated layers [50]. Bistritzer and MacDonald found coherent interlayer contact resistances changing by 16 orders of magnitude as the rotation angle is changed by 30° [56]. Recent calculations of the phonon-mediated, interlayer conductance indicate that the phonon-mediated current is a significant interlayer transport mechanism at room temperature [57]. The phonon-mediated current has a weaker dependence on rotation angle. At room temperature with a Fermi level 260 meV above the Dirac point, the interlayer resistance was found to smoothly vary from 50 $\Omega\mu\text{m}^2$ at small rotation angles of a few degrees to 330 $\Omega\mu\text{m}^2$ at a rotation angle of 30° [57].

In addition to the electronic properties, the unique chiral nature of quasi-particles in graphene results in a novel quantum Hall effect [17–19] that opens a new possibility for spintronic applications [58, 59]. The electron motion in misoriented graphene can be further modulated by the application of an external perpendicular magnetic field (B-field) with formation of Landau levels (LLs) residing permanently at the Dirac points even with varying magnetic field. [16, 60] Recently several researchers [58, 61–66] found that GNRs could have interesting magneto-electronic properties such as giant magnetoconductance modulation (i.e., a large conductance difference between two magnetic configurations). For example, two zigzag GNR (ZGNR) based devices exhibiting a giant magnetoresistance ratio (GMR) have been proposed [58,67] where in one device [58], the GMR is configured with two ferromagnetic (FM) states of ZGNR electrodes in parallel vs. antiparallel alignments and a magnetoresistance ratio (MR) (%) change of 10,000% is reported for a 32-ZGNR; in the other device, it is configured between a FM and an antiferromagnetic (AFM) state of a ZGNR controlled by applying an external B-field. [67] Saffarzadeh and Asl [66] also showed that the planar FM/GNR/FM junction with zig-zag (armchair) interfaces exhibits a high (low) MR ratio. Hill et al. [62] experimentally observed a 10% MR ratio in a GNR based spin-valve device, where a 200 nm GNR was connected to NiFe contacts.

A negative MR of nearly 100% was observed at low temperatures, with over 50% remaining at room temperature [63]. The negative MR can also be achieved [68] in intrinsic graphene and a nonmonotonic MR can be obtained in extrinsic graphene with a parallel magnetic field. All these studies stimulate further investigation of the transmission between misoriented graphene layers under an applied magnetic field. Since the transmission is governed by quantum interference of the relative phases of the wavefunctions of the two layers and a magnetic field modifies the phase of the electronic wavefunction, one might expect that the transmission could be sensitive to an applied B-field. Therefore understanding the effect of magnetic field on the transmisison between misoriented graphene layers is required to fully understand the design requirements of such structures.

1.2 Overview

In this dissertation, the electronic and magneto-electronic properties of graphene and bilayer graphene are explored. To explore the electronic properties, in chapter 2, we describe calculations based on the semi-empirical extended Huckel theory and the NEGF formalism. Significant bandgap openings are obtained in all of the various graphene based structures. The external bias has a significant effect on the bandstructure of bilayer GNRs. Based on this property we consider a device consisting of two stacked monolayer AGNRs designated as a s-AGNR device. Electron transport through the s-AGNR device shows negative differential resistance (NDR) behavior that decreases with increasing ribbon width. We also investigate a graphene nanomesh consisting of a nano-patterned graphene sheet with uniformly distributed holes in which the band gap can be tuned.

Obtaining a modest bandgap of a few hundred meV in graphene generally comes

at the expense of strongly degraded electron mobility, and it requires difficult lithography. In chapter 3, we propose an unconventional biasing approach of modulating the current voltage characteristics ($I-V$) without a bandgap. An atomistic model based on the extended Huckel theory (EHT) coupled with the non-equilibrium Green's function formalism (NEGF) is used for electronic transport calculations. The calculated $I-V$ characteristics of a single layer and bilayer GFET show NDR behavior at room temperature which originates from the symmetric band structure of graphene. The theoretically calculated NDR in a GFET is also supported by experimental results, and it allows for construction of non-Boolean computational architectures using gapless graphene [1]. Our atomistic modeling shows that the NDR appears not only in the drift-diffusion regime but also in the ballistic regime at the nanometer-scale although the physics changes.

Finally in chapter 4 we study the magneto electronic properties of misoriented stacked graphene layers applying a vertical magnetic field. We consider a simple device structure with two misoriented bilayer graphene nanoribbons (mBGNR) twisted at an angle of 30°. We investigate the interlayer transmission of the mBGNR structure in the presence of a uniform magnetic field and describe how the interlayer transmission of the mBGNR structures is modulated by the magnetic field. We also investigate the magnetoconductance (MC) effect in the mBGNR device and obtain a very large MC effect tunable by an applied magnetic fielld. The observed MC property in this work is intrinsic unlike typical MC effects which are related to spin asymmetric scattering. Finally we investigate the dependence of the MC effect on temperature. Although the electronic and transport properties in a single GNR under a magnetic field have been extensively studied, we are not aware of any work addressing the effect of magnetic field on the inter-layer transport properties of a misoriented large graphene structure, and our study represents a first step in this direction.

Chapter 2

Bandgap Engineering and Quantum transport in Graphene

Graphene, an allotrope of carbon, attracts considerable attention due to its excellent electrical and thermal properties. Effective use of graphene in digital applications is limited due to its lack of an energy gap in its electronic spectra. Several methods have been proposed to open up a band gap such as pattering graphene into a dot (i.e. 0 D), ribbons, (i.e. 1D), epitaxial growth etc. However, lateral confinement (0D, 1D) suppresses the intrinsic mobility of graphene. Also some of the methods require complex lithographic processes. An efficient method of opening a band gap preserving the 2D structure and mobility of graphene is needed. We investigate various approaches to induce a band gap. We start with a typical armchair graphene nanoribbon (AGNR) and propose a stacked structure of monolayer graphene (s-AGNR). The stacked structure shows that a tunable bandgap can be induced in s-AGNR by application of a potential difference between the two layers. The simplest geometry for creating such a potential difference consists of two overlapping single layer graphene nanoribbons. Numerical simulations, based on semi-empirical Extended Huckel theory (EHT) and

the non-equilibrium Green's function formalism, show that transmission through such a structure has a strong dependence on applied bias. The simulated current voltage characteristics mimic the characteristics of a resonant tunneling diode featuring negative differential resistance. The bandgap and width of the nanoribbons affect the current voltage characteristics. In particular, the peak to valley current ratio (i.e., I_{on}/I_{off}) decreases with increasing width of the nanoribbons. Finally, a 2D structure of graphene patterned with a periodic array of nano holes is investigated. Band structure calculations of this structure are carried out with EHT as functions of structural parameters, including the hole size and the hole to hole distances. Our results suggest that the bandgap opening is a result of quantum confinement at the nanomesh necks. The effective mass is also calculated as a function of the nanomesh neck widths.

In this chapter, we start begin an AGNR and study the effects of the width of the AGNR on the bandgap opening. We also study the bandstructure of AB stacked nanoribbons. We observe that the bandgap increases with applied bias between the bilayer region. Knowing the electronic strucure of single and bilayer AGNRs, we consider a stacked AGNR consisting of two single layer AGNRs stacked on top of the each other. Each GNR is independently contacted such that one GNR is held at ground while the other has a bias applied to it. Independently contacting the top and bottom GNR maximizes the voltage drop between them. Assuming that the majority of the potential drop occurs between the two GNRs, then the potential difference between the two GNRs is the applied bias. Simualted $I-V$ characteristics using semi-empirical EHT and the non-equilibrium Green's function formalism (NEGF) shows an NDR effect. The width of the AGNR has a significant effect on the electron transport. In particular, the on/off ratio decreases with increasing width of the ribbons.

Finally we report another concept of inducing a bandgap on a new graphene based structure. The structure consists of densely patterned array of holes in graphene. The

patterning of dense arrays of ordered holes still remains a significant challenge. In experimental work conducted by Bai et al. [69]. the nanomeshes were prepared using block copolymer lithography and can have variable periodicities and neck widths as low as 50 Å. We theoretically show that we can have modest bandgap comparable to that of AGNR and can be tuned by varying various parameters such as periodicity, neck width and hole diameter.

2.1 Theoretical formalism

Semi-empirical Extended Huckel Theory (EHT) is used for the electronic structure calculations. The dispersion relation $(E - k)$ is derived using the calculated Hamiltonian and overlap matrix from the Huckel code. Finally we calculate current using Non-equilibrium Green's functions (NEGF) formalism. We optimize our structures using ab-initio Density Funtional theory (DFT).

2.1.1 Extended Huckel theory

The basis functions in Extended Huckel theory (EHT) are related to the atomic orbitals i.e., the Slater-type orbitals (STOs). STOs allow the overlap matrix S_{ij} to be calculated efficiently [70]. The individual molecular orbital wave functions are approximated by a linear combination of STO's as follows

$$\phi_{nlm}(\mathbf{r}) = \sigma r^{n-1} e^{-\zeta r} Y_{lm}(\theta, \varphi)(= STO) \tag{2.1}$$

where spherical coordinates r, θ, ϕ have been used. n (= 1, 2, . . .), l (= 0, 1, . . . , n-1), and m (= -l, -l + 1,. ..., 0, 1, . . . , l-1, l) are the principal, angular momentum, and magnetic quantum numbers, respectively. The $Y_{lm}(\theta, \varphi)$

are the real-valued spherical harmonics. ζ is the orbital exponent and is related to the effective nuclear charge. The nuclear charge is partially shielded by electrons in the core of an atom. σ is the normalization constant and obtained from

$$\sigma^2 \int_0^\infty (r^{(n-1)} e^{-\zeta r})^2 r^2 dr = 1 \Longrightarrow \sigma = \frac{(2\zeta^{\frac{n+1}{2}})}{\sqrt{(2n)!}}. \tag{2.2}$$

The Hamiltonian elements are constructed using the Huckle principle. The diagonal elements or on-site energies are taken from experimental values of electronic 'hard ness' i.e., the difference between the ionization potential and the electron affinity. The off-diagonal matrix elements are determined directly from the following equation

$$\begin{aligned} H_{ii} &= E_i \\ H_{ij} &= \frac{1}{2} K_{EHT}(E_i + E_j) S_{ij} (i \neq j) \end{aligned} \tag{2.3}$$

K_{EHT} is an fitting parameter taken as c =2.8 [71]. E_i and E_j are the on-site energies. One important assumption within EHT is that the hopping matrix elements H_{ij} depend linearly on the overlap matrix S_{ij} given by

$$S_{ij} = \int \varphi_i^*(\mathbf{r}) \varphi_j(\mathbf{r}) d^3 r \tag{2.4}$$

where $\varphi_i(\mathbf{r})$ and $\varphi_j(\mathbf{r})$ are the STOs basis functions. Thus, the effect of bond length variation is included in the overlap matrix. The device Hamiltonian, overlap matrix, and the device-to-lead coupling matrices are extracted and used for the NEGF algorithm to calculate transmission coefficients.

We use spin-restricted EHT for the electronic structure calculations. For electronic band-structure, the H and S matrices of the infinite GNR, graphene sheet and

graphene bilayer are transformed into reciprocal k-space as

$$H(\vec{k}) = \sum_{n=1}^{N} H_{mn} e^{i\vec{k}(\vec{d}_m - \vec{d}_n)} \tag{2.5}$$
$$S(\vec{k}) = \sum_{n=1}^{N} S_{mn} e^{i\vec{k}(\vec{d}_m - \vec{d}_n)}$$

where $\vec{k}$ is the reciprocal lattice vector of the Brillouin zone. $\vec{k}$ is one dimensional for GNRs and two dimensional for for single and bilayer graphene sheets. The index m represents the center unit cell and n represents the neighboring unit cells, and $\vec{d}_m - \vec{d}_n$ is the relative displacement. The energy eigenvalue spectrum at a specific k point is computed from the generalized eigenvalue equation,

$$H(k)\psi(k) = E(k)S(k)\psi(k). \tag{2.6}$$

2.1.2 Non-equilibrium Green's functions(NEGF)

In this study, we use a non self-consistent EHT/NEGF approach where the NEGF calculation operates as a post-processor to the EHT calculation as shown in Fig. 2.1.

The transmission calculation is performed in the three steps. In general, the calculation starts with a semi-empirical EHT calculation of an ideal periodic bulk material corresponding to the source and drain leads. The contact Hamiltonian and the overlap matrix elements are stored for calculating the surface self-energies. The second step is to run the EHT calculation of a contact - device - contact structure. After the calculation, we store the Hamiltonian and overlap matrix elements of the device structure and the device to lead coupling matrices. For the third step, the saved matrix elements are used to calculate the surface self-energies, the Green's function of the device, and transmission coefficient.

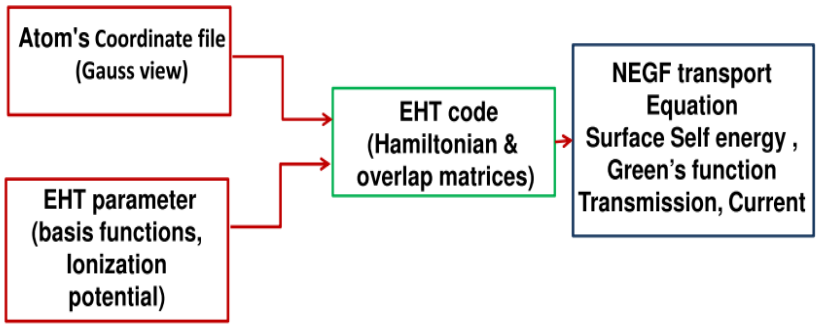

Figure 2.1: Flowchart diagram of EHT/NEGF

As an example of this method, consider the stacked AGNR (s-AGNR) geometry shown in Fig. 2.2. This geometry consists of two single layer GNRs with one placed on top of the other.

Each GNR is independently contacted such that one GNR is held at ground while the other has a bias applied to it. For NEGF, we define the atoms that lie between the two dotted vertical lines in Fig. 2.2 as the 'device.'

The NEGF calculation of the s-AGNR structure (for example, Fig. 2.2), begins with a calculation of the GNR contact surface self-energies, $\Sigma^L_{1,1}$ and $\Sigma^R_{N,N}$. A decimation technique [72, 73] is adopted to calculate the surface self-energies from a *periodic* infinite GNR, consisting of an eight-atomic-layer unitcell along the growth direction. The GNR shown in Fig. 2.3, is divided into eight atomic layered supercells or unit cells. Non-zero matrix elements of a given atomic layer extend to the left and right 8 atomic layers, or one unit cell of the GNR.

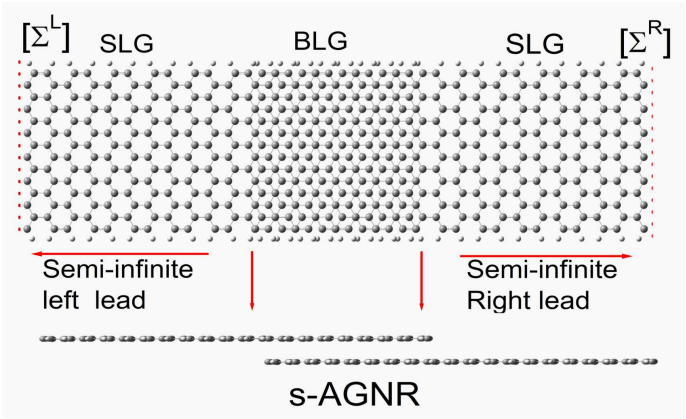

Figure 2.2: (top) Schematic diagram of s-AGNR device including the contact surface self energies. The region inside the vertical line is the device region. (bottom)Side view of the structure

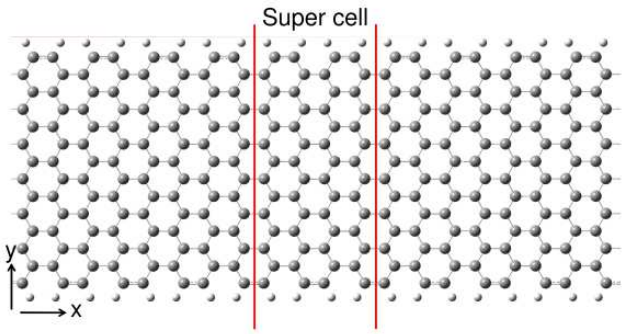

Figure 2.3: Schematic of hydrogen passivated armchair GNR. The region inside the vertical lines is supercell/unitcell. The GNR is a periodic construction of the supercell.

The GNR Hamiltonian matrix elements are grouped into inter-cell subblocks $t_{n,n\pm1}$ and intra-cell subblocks $D_{n,n}$. We define inter-cell matrix element block $\tilde{t}$, for equilibrium conditions, as

$$\tilde{t}_{n,m} = t_{n,m} - (E + i\eta)S_{n,m} \tag{2.7}$$

where $S_{n,m}$ is the overlap matrix between non-orthogonal orbitals in cells n and m, E is the energy, η is a convergence factor that is non-zero only in the contacts. For nonequilibrium conditions, the matrix elements of the potential from the applied bias, $U_{n,m}$, are added to the right hand side of Eq. 2.7 as discussed at the end of this chapter. For calculations presented below, $\eta = 10$ meV is typically used.

The equations that we solve for the surface Green's function of left lead (unit cell number 0) are

$$\begin{aligned}
\tilde{t}_i &= \tilde{t}_{i-1}\left[(E + i\eta)S_{0,0} - D_{i-1}\right]^{-1}\tilde{t}_{i-1} \\
\tilde{t}_i^{\dagger} &= \tilde{t}_{i-1}^{\dagger}\left[(E + i\eta)S_{0,0} - D_{i-1}\right]^{-1}\tilde{t}_{i-1}^{\dagger} \\
D_i &= D_{i-1} + \tilde{t}_{i-1}\left[(E + i\eta)S_{0,0} - D_{i-1}\right]^{-1}\tilde{t}_{i-1}^{\dagger} \\
&+ \tilde{t}_{i-1}^{\dagger}\left[(E + i\eta)S_{0,0} - D_{i-1}\right]^{-1}\tilde{t}_{i-1} \\
D_i^s &= D_{i-1}^s + \tilde{t}_{i-1}\left[(E + i\eta)S_{0,0} - D_{i-1}\right]^{-1}\tilde{t}_{i-1}^{\dagger}
\end{aligned} \tag{2.8}$$

Equations (2.8) define an iterative Hamiltonian for a chain of principal layers (unit cells) with lattice constant 2^ia, where a is the zero-order lattice constant and i is the iteration number. $\tilde{t}$ and $\tilde{t}^{\dagger}$ are the Hamiltonian matrices coupling 8-atomic-layers or one unit cell to ether side of the principal unit cell. D_i^s is the surface layer block at iteration i. For the surface Green's function of the left lead, the calculation starts with the initial guess $D_0 = D_0^s = D_{0,0}$, $\tilde{t}_0 = \tilde{t}_{0,-1}$, and $\tilde{t}_0^{\dagger} = \tilde{t}_{-1,0}$. The surface Green's function convergence, which typically requires approximately 12 iterations, is met

when the maximum value of any element of the $\tilde{t}$ matrix is less than 10^{-10}. After convergence of Eqs. (2.8) at iteration n, the surface Green's function on the left lead is

$$g_{0,0} = [ES_{0,0} - D_n^s]^{-1} \tag{2.9}$$

The same procedure as above applies for the surface Green's function of the right lead. In non equilibrium, however, a potential matrix, $-U_{n,m}$ is added to the term inside the square brackets in Eq. (2.8) and (2.9) for a given source/drain bias applied at the right lead. Once the surface Green's functions $g_{0,0}$ and $g_{N+1,N+1}$ are converged, the self-energy matrices are calculated from the expressions

$$\begin{aligned} \Sigma^{\ell} &= \tilde{t}_{1,0} g_{0,0} \tilde{t}_{0,1} \\ \Sigma^{r} &= \tilde{t}_{N,N+1} g_{N+1,N+1} \tilde{t}_{N+1,N} \end{aligned} \tag{2.10}$$

where Σ^{ℓ} and Σ^{r} are the surface self-energies for the left and right GNR contacts respectively. This method is described in detail in Ref. [74–76].

For the NEGF calculation, we divide the s-AGNR structure into blocks. We number these blocks such that blocks $\{-\infty, \ldots, 0\}$ lie in the left contact, blocks $\{(N+1), \ldots, \infty\}$ lie in the right contact and blocks $\{1, \ldots, N\}$ lie in the device. The self-energies are placed on the outer most blocks (1 and N). At each energy E, the retarded Green's function [77] is calculated from

$$G^R(E) = \left[ES_D - H_D - U_D - \Sigma^{\ell} - \Sigma^{r}\right]^{-1} \tag{2.11}$$

where the subscript D indicates the 'device' region of structure.

At each energy E, the transmission is calculated from

$$T(E) \;=\; \mathrm{tr}\left\{\Gamma^{L}_{1,1} G^{R}_{1,N} \Gamma^{R}_{N,N} G^{R}_{1,N}\right\} \tag{2.12}$$

or

$$T(E) \;=\; \mathrm{tr}\left\{\Gamma^{L}_{1,1}\left[A_{1,1} \;-\; G^{R}_{1,1}\Gamma^{L}_{1,1}G^{A}_{1,1}\right]\right\} \tag{2.13}$$

where $\Gamma^{L}_{1,1} = i\left(\Sigma^{\ell} - \Sigma^{\ell\dagger}\right)$, $\Gamma^{R}_{N,N} = i\left(\Sigma^{r} - \Sigma^{r\dagger}\right)$, and $G^{A} = \left[G^{R}\right]^{\dagger}$. Expression (2.12) is the more commonly known expression for transmission and corresponds to what has become known as the Fisher-Lee [78] form of the transmission coefficient although the expression was written down 10 years earlier by Caroli et al. [79]. Eq. (2.13) is more numerically efficient since it only requires the calculation of the upper corner block of G^{R}.

To understand the spatial extent of states at a given energy, we calculate and plot the covariant spectral function [80]

$$A_{i}(E) \;=\; -2\,\mathrm{Im}\left[\mathrm{tr}_{i}\left(SG^{R}(E)S\right)\right] \tag{2.14}$$

where the trace is over the basis states associated with atom i. The large scale matrix inversions and multiplications, required for calculating the self-energies and device transmission, are done using MATLAB code.

To calculate current, a non self-consistent approach is used. A bias is applied across the left and right contact leads. The semi-infinite right contact lead (GNR) includes one unit cell of GNR in the Hamiltonian and is kept at zero bias. The semi-infinite left lead includes one unit cell of GNR in the Hamiltonian and is kept at the applied bias. The matrix elements of the potential energy matrix U are calculated

using the following equation

$$\langle i,\alpha|U|j,\beta\rangle = -eS_{\alpha_i,\beta_j}\left[V_b(\mathbf{r}_i)+V_b(\mathbf{r}_j)\right]/2. \tag{2.15}$$

where, the indices i and j label the atoms and indices α and β label the basis orbitals. S_{α_i,β_j} is the overlap matrix $\langle i,\alpha|j,\beta\rangle$. The approach captures the Stark effect, but not nonequilibrium self consistency.

For transmission calculation the energy grid is evenly spaced between $\mu_L - eV_b - 15kT$ to $\mu_R + 15kT$ where kT is the thermal energy and μ_L and μ_R are the Fermi levels of the left and right contacts respectively. Once the transmission is calculated, the coherent current is then calculated from,

$$I = \frac{2e}{\hbar}\int \frac{dE}{2\pi}T(E)\left[f(E-\mu_R) \; - \; f(E-(\mu_L - eV_b))\right] \tag{2.16}$$

where, $f(E)$ is the Fermi function.

In brief, the NEGF calculation begins by obtaining self-energies of the semi-infinite leads. The divided 'device' supercell is then used to form the Hamiltonian matrix, H_D, which in turn is used to obtain the Green's function. The transmission coefficient and current are calculated from this Green's function.

2.2 Results and Discussion

In this section, we discuss our simulation results carried out on three different graphene structures.

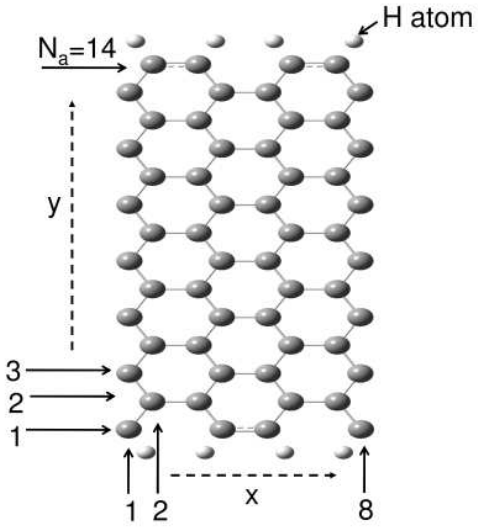

Figure 2.4: H-passivated Graphene supercell containing 14x8 atomic layers of carbon atoms. This figure also illustrates the numbering scheme.

2.2.1 Armchair Graphene Nano Ribbon (AGNR)

Graphene nanoribbons (GNRs) are quasi one-dimensional (1D) structures patterened from graphene sheet in particular orientations. They are characterized by the alignment of the edge atoms, namely zigzag GNR (ZGNR) and armchair GNR (AGNR). It is predicted that all zigzag GNRs are metallic with localized states on the edges [81,82] while armchair GNRs are either metallic or semiconducting, depending on their widths [83]. GNR's have different electrical properties compared to graphene sheets due to quantum confinement as well as the abrupt termination at the edges. Throughout the chapter, we use the naming convention followed in Ref. [3] where a N-carbon-atomic-layers wide AGNR is referred to as a N-AGNR. Hence, the supercell of a 14-AGNR contains 14 carbon atoms in the y-direction as shown in figure 2.4. For example, Fig. 2.3 illustrates a 14-AGNR where the region inside the vertical lines is the

supercell. These supercells are used along with periodic boundary conditions along x axis to relax the AGNRs which in turn are used in the band structure calculation. In all of our calculations, we generated GNRs using a $c-c$ bond length of 1.4617 Å obtained from a geometry optimization using the DFT FIREBALL code.

The simulated band structure of a 14-AGNR is shown in figure 2.5(a). The structure shows a typical linear dispersion having a small band gap of 0.084 eV. The transmission coefficient ($T(E)$) of passivated armchair nanoribbon under zero bias is shown in figure 2.5 (b) with several integer steps and narrow jumps. These steps are consistent with the band structure generated by our model. In such a perfect 1D crystal without any defects, each Bloch state can propagate through the junction without any classical resistance and contribute a unit of quantum conductance for the total transmission spectrum. The integer steps in the transmission spectrum indicate the number of the conducting channels or bands at that energy For any energy value under consideration, one can accurately predict the transmission coefficient for the perfect quasi-1D crystal simply by counting the number of bands in the electronic structure.

The edge of armchair nanoribbons used in our simulation are hydrogenated to eliminate surface states. Because every atom on the edge has one unsaturated dangling bond, the characteristics of the $c-c$ bonds at the edges can change GNRs' electronic structure dramatically [84, 85]. To determine the band gaps of GNRs at nanometer scales, edge effects should be considered carefully. The change of edge bond length and angle can lead to considerable variations of electronic structure, especially within the low-energy range. Therefore in this work, all edge carbon atoms of GNRs are passivated by hydrogen atoms. Figure 2.5 (c) shows the $E-k$ diagram for an unpassivated GNR for comparison. Our result shows that in case of unpassivated AGNR, the energy dispersion relation deviates from that of passivated structures.

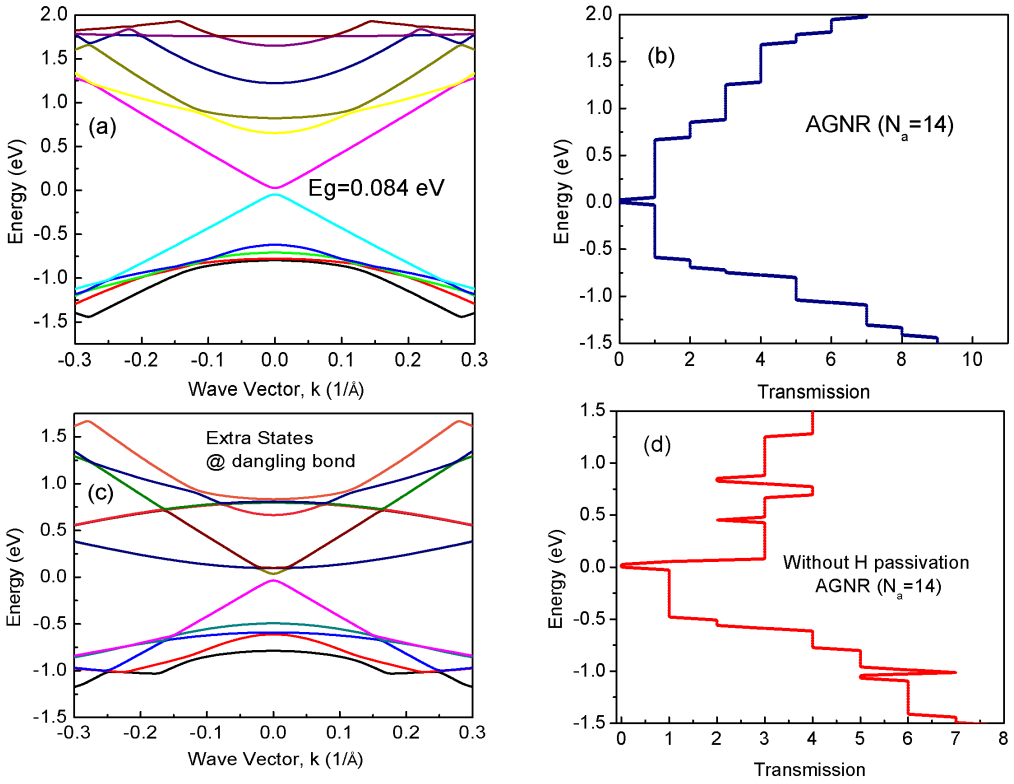

Figure 2.5: (a) Electronic structure of passivated 14-AGNR (b) Transmission spectrum for 14-AGNR (c) Edge states for unpassivated 14-AGNR, i.e. edges without H atoms(d) Transmission spectrum for unpassivated 14-AGNR.

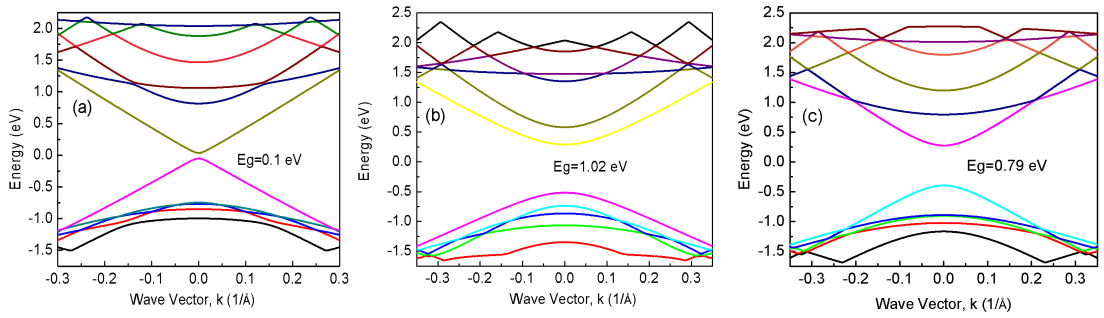

Figure 2.6: Electronic structures of armchair GNRs with various widths (a) Na = 11 (b) Na = 10 (c) Na = 9, respectively.

The calculated $T(E)$ is plotted in figure 2.5 (d), showing extra modes generated due to dangling bonds. It clearly demonstrates the beneficial effect of H-passivation in eliminating edge states.

Now we will discuss the effect of varying the width on the bandstructure. An AGNR with the width of N_a = 3n + 2 where n is an integer is generally metallic, and otherwise it is semiconducting [81]. Figure 2.6(a-c) shows the calculated energy dispersion for an AGNR having different widths of N_a = 11, 10 and 9 respectively. The $E-k$ relation of an 11-AGNR (i.e., $N_a = 11$), shows inear dispersion around the Γ point and the lowest conduction band and the upmost valence band almost touch at the Dirac point leading to the metallic behavior. Our simualtion shows that both 9-AGNR and 10-AGNR have a significant bandgap. The 10-AGNR shows the largest bandgap of $\sim$ 1 eV with a parabolic dispersion around Γ as shown in fig. 2.6(b) .

The electronic structures of AGNRs depend strongly on their widths. Due to the quantum confinement, the spectrum breaks into a set of subbands and the wave vector along the confined direction becomes discretized. As the width gets larger (N_a = 14, 17 and so on), the quantum confinement becomes less important and the 1D nanoribbons tend to behave like 2D graphene. The electron effective masses calculated

from the band structures are listed in table 2.1. The small value of effective mass is expected for graphene as ideally it consists of massless particle termed as Dirac fermion. For each type of AGNR, the effective masses are inversely proportional to the width with a different proportionality constant.

Table 2.1: Effective Mass of Different AGNRs

AGNR Type	Atomic layers (N_a)	Effective mass (m^*)
3n	9	$0.132m_0$
3n	12	$0.12m_0$
3n	15	$0.095m_0$
3n+1	10	$0.16m_0$
3n+1	13	$0.121m_0$
3n+2	11	$0.019m_0$
3n+2	14	$0.016m_0$

In figure 2.7, we plot the variation of bandgap with width of AGNR. The variations in energy gap of three distinct family 3n, 3n+1 and 3n+2 AGNRs. where n = 1, 2, 3 etc are investigated. We observe that the electronic structure of perfect armchair GNRs strongly depends on the width of the ribbon. The bandgap opening follows a inverse relation with ribbon width as expected. A bandgap opening of 1.1 eV can be achieved for 10-AGNR. Our simulated results are compared with other calculations using a first-principles approach [3], and our own calculations using the DFT codes FIREBALL and VASP. All of the results are plotted in the same figure shown in Fig. 2.7. The EHT results are in good agreement with those from other models.

2.2.2 Stacked Armchair graphene nanoribbon (s-AGNR)

In the previous section, we discussed the bandgap opening in an AGNR by constraining one of the dimensions of graphene (i.e. the width). In this section, we consider another way to introduce a band gap by stacking two GNRs. We stack two 14-AGNR

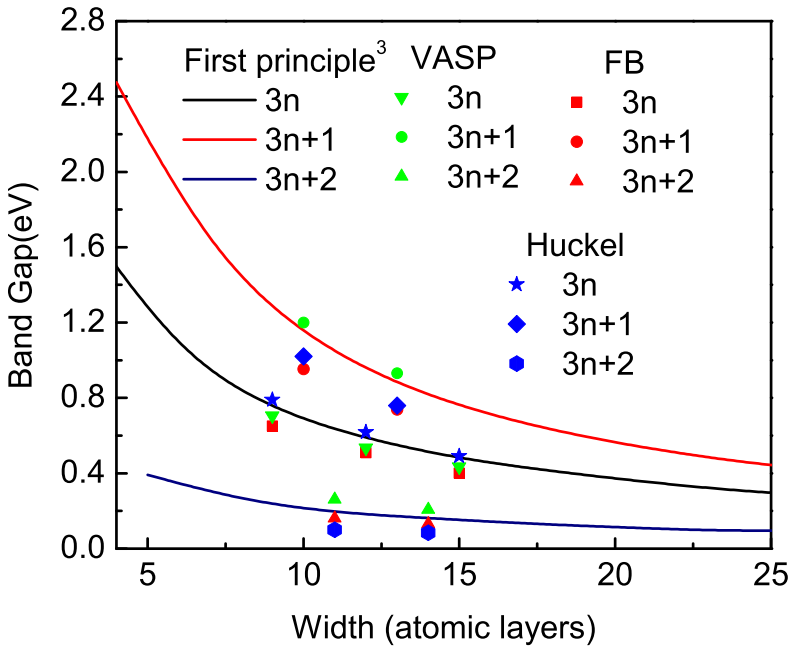

Figure 2.7: Calculated bandgap as a function of AGNR width (N_a) (3n, 3n+1, 3n+2 where n is a positive integer). Comparing EHT results with DFT Fireball, VASP and first principal calculations [3].

in AB stacking on top of each other constructing a bilayer GNR. The external bias, V_b is applied in between the top and bottom GNRs. The effect of bias was taken into account by shifting the potential energy of all the atoms of the top GNR by $-eV_b$, where e is the charge of an electron. This is done by changing the Hamiltonian matrix elements of the top layer. The matrix elements of V_b were calculated using Eq. 2.15. The band structures of the s-AGNR ($N_a = 14$) at both unbiased and biased conditions are shown in Figs. 2.8 (a) and (b), respectively. Although the single layer has a band gap of 0.84 meV, the stacked AGNR has significantly smaller band gap of 0.05 eV. The band structure changes significantly with applied bias voltage as shown in Fig.2.8(b). Under an applied bias of 0.4V, the induced bandgap is 0.187 eV (see in Fig. 2.8(b)), and the bandstructure shows a non-linear dispersion relation.

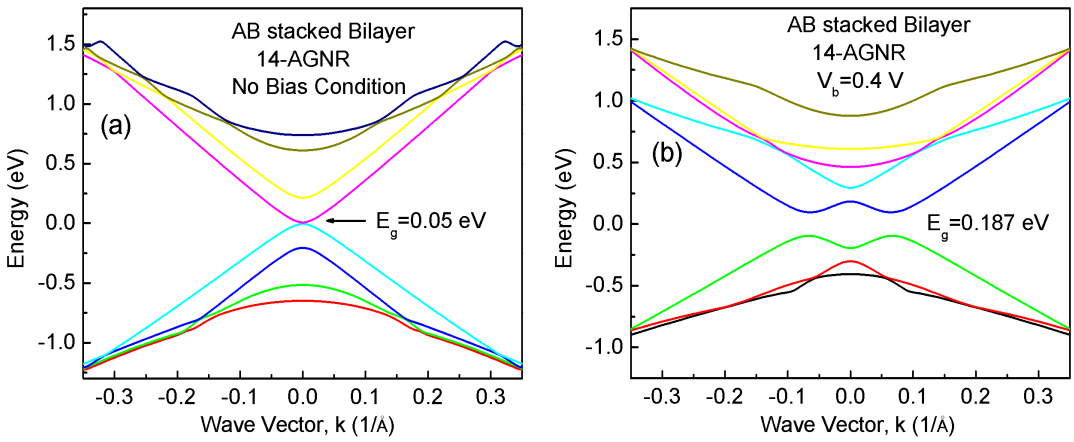

Figure 2.8: Band structure of s-AGNR: (a) no bias and (b) at bias, $V_b = 0.4V$. A bandgap of 0.187 eV is opened as a result of 0.4 V bias. Fermi level is at 0 eV.

Now we will discuss the bandgap modulation with applied V_b. Figure 2.9 shows the band gap of a s-AGNR as a function of V_b. The plot shows the possibility of band gap tunability of 0.05 eV to 0.205 eV over an applied bias ranging from 0 to 0.8V respectively, after that induced bandgap saturates and becomes independent of

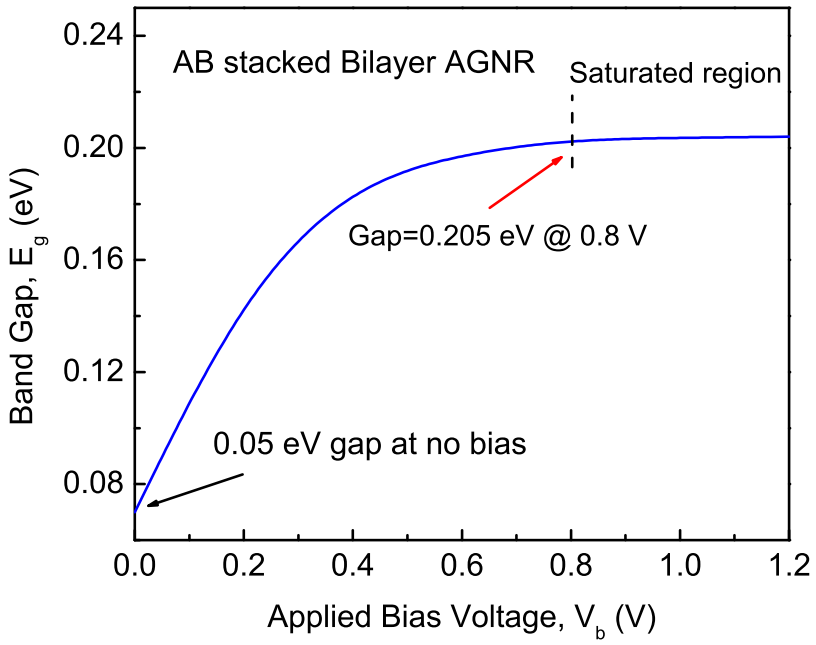

Figure 2.9: Band gap variation of s-AGNR as a function of applied bias.

applied V_b. Since band gap increases with bias, negative differential resistance (NDR) could occur in bilayer graphene devices.

In order to study the possibility of a NDR effect in a s-AGNR device, we investigate a two terminal device using a stacked AGNR as the channel material. The schematic of the device is shown in Fig. 2.10. The device consists of two hydrogen passivated 14-AGNRs overlapped in the central region with a vertical separation of 3.35 Å. The length and width of the overlap region of the device are 18 Å and 17 Å, respectively, and the total length of the structure is 67 Å. A positive bias voltage, V_b, is applied to the left contact (the top AGNR) with respect to the right contact (the bottom AGNR). The independent contacts to the top and bottom GNRs maximize the voltage drop between them.

The simulated $I - V$ characteristic for the s-AGNR is shown in Fig. 2.11. The

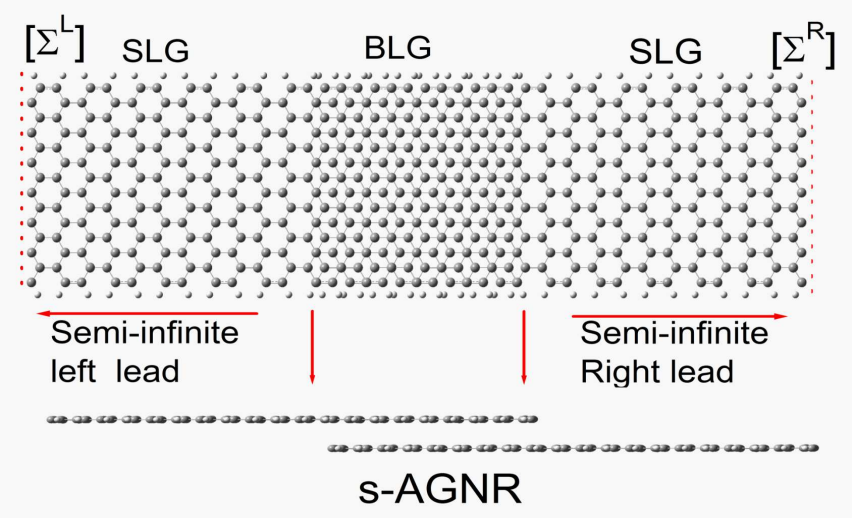

Figure 2.10: Schematic diagram of s-AGNR device. The device region is an AB stacked bilayer GNR connected to SLG, All GNRs are Hydrogen passivated

current decreases beyond a certain applied bias voltage exhibiting negative differential resistance (NDR). The peak occurs at 0.4 V and the valley minimum occurs at 0.7 V where the peak (I_{on}) and valley currents (I_{off}) are 10 μA and 2 μA, respectively. Transport calculations through the same system were performed with FIREBALL [86] as shown in the same figure, and they are in good agreement with our calculation.

To explain the NDR effect, we simulate the transmission coefficients ($T(E)$) (see Fig. 2.12) as a function of electron energy at no-bias and two different bias voltages of $V_b = 0.38$ V and 0.7 V. The coherent current at any bias is proportional to the area under the transmission curve bounded by the Fermi levels of the contacts. From this plot, it is clear that a potential difference between the two GNRs strongly suppresses the overall transmission. At the valley minimum of $V_b = 0.7$ V, a maximum suppression occurs over an energy window of 0.7 eV as shown in Fig. 2.12 and the overall

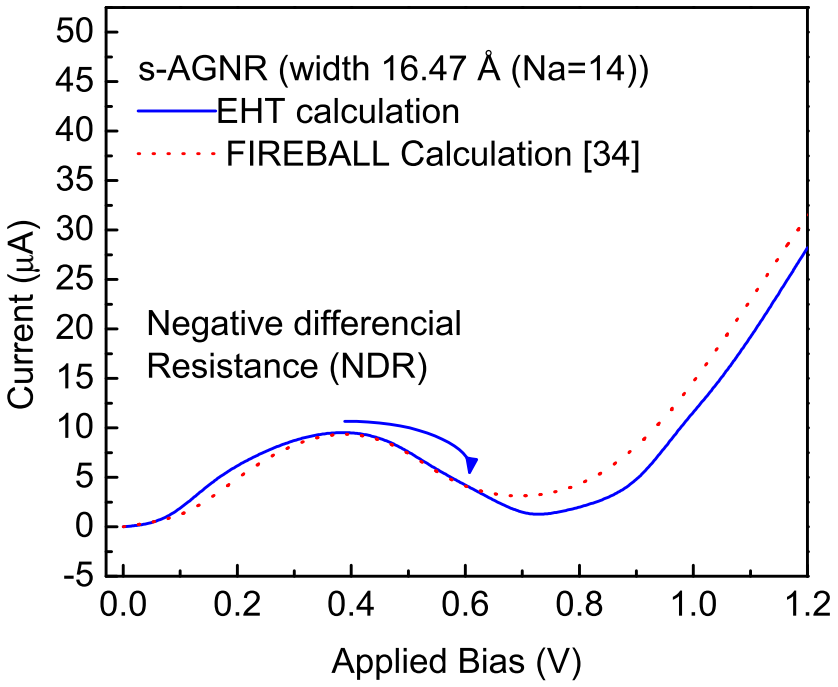

Figure 2.11: Simulated $I-V$ characteristics of AB-stacked GNR. The minimum and maximum current is at 0.7 V and 0.38 V respectively.

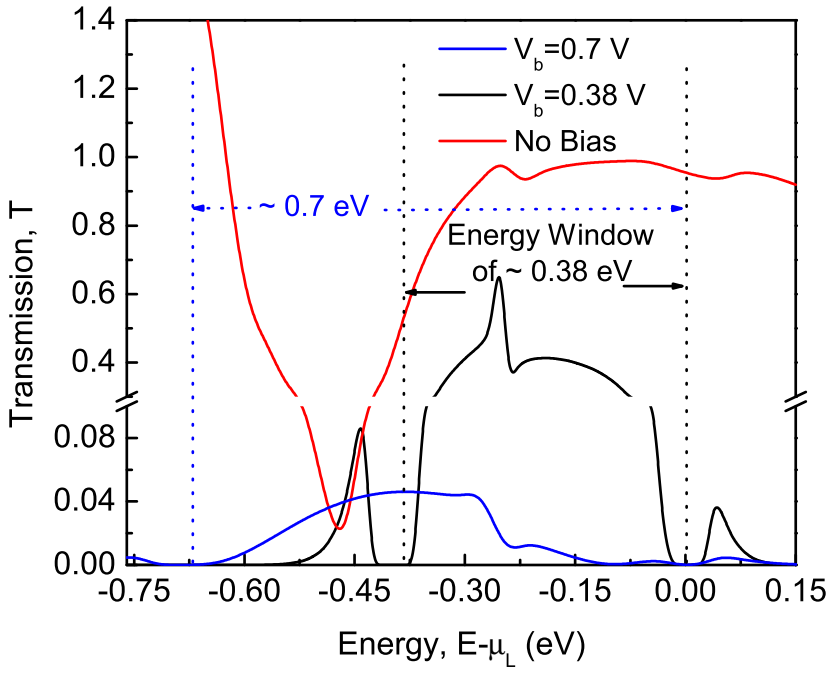

Figure 2.12: Transmission as a function of energy for an s-AGNR at no bias and a bias of $V_b = 0.38$ V and $V_b = 0.7$ V. The left and right vertical lines represent the quasi-Fermi levels of the left and right contacts ($V_b = 0.7$ V, 0.38 V) respectively.

trend is in good agreement with Ref. [86]. The low transmission near E = 0 eV and E = -0.38 eV are due to the bandgap of the GNR leads. From the figure we can see that the transmission for $V_b = 0.7$ V is smaller compared to that of $V_b = 0.38$ V. This implies that the area bounded by the fermi levels and transmission curve is smaller for $V_b = 0.7$ V resulting in less current. The current phenomenon could be explained as resulting from the suppression of the coherent transition due to the mismatch of modes in the contacts and the bilayer channel region of the device. Multiple reflection can occur at the edge of the overlap region due to potential discontinuity. When the bias voltage is increased from 0.39 V to 0.7 V, the possibility of wave vector mismatch

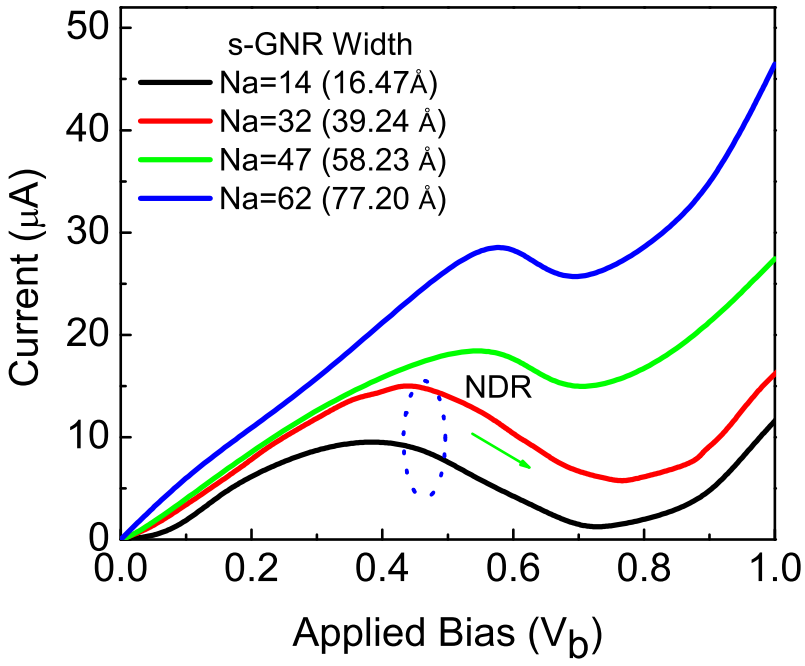

Figure 2.13: $I - V$ characteristics of s-AGNR devices varying width (N_a = 14, 32, 47, 62).

is increased resulting strong suppression of transmission. Beyond 0.7 V, the current increases with applied voltage since the transmission increases as a result of excited subbands of the leads. The simulations of a model structure with AB stacking provide proof-of-concept that NDR can occur in such structures.

Now we will discuss the effects of GNR width (W) on NDR. We consider three structures with W = 39.24 Å, 58.23 Å and 77.2 Å. The width of the GNRs of these structures are chosen to be (3n + 2) to minimize the effects of bandgap resulting from finite width. The $I - V$ characteristics of the proposed bilayer structure show a significant dependence on W as indicated in Fig. 2.13. The peak current to valley current I_{on}/I_{off} ratio decreases with increasing ribbon width. For larger W, $T(E)$ increases as more channels (excited subbands) are available. The multiple subbands

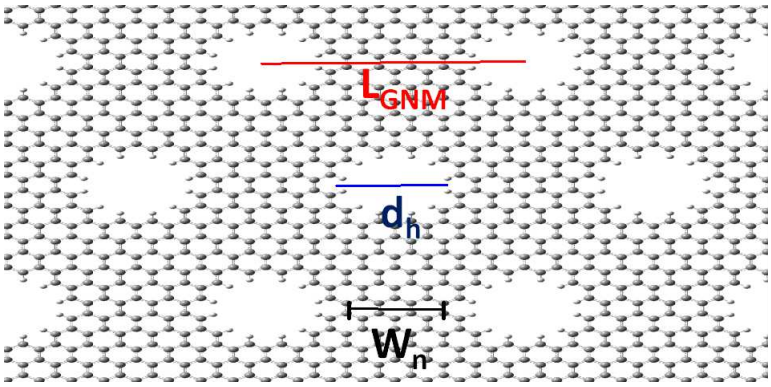

Figure 2.14: Basic structure of GNM showing L_{GNM}, W_n and d_h

are close and may provide multiple path to assist the current flow. An electron from the left contact has a higher probability to transport through the device. As a result the current through the device increases with the bias voltage, decreasing the current on/off ratio.

2.2.3 Graphene Nano Mesh (GNM)

All these proposed garphene structures (AGNRs and s-AGNR) require high resolution lithography which may be difficult experimentally. With that in mind, we model and simulate a graphene nanomesh (GNM) by patterning 'nano-holes' on a graphene sheet. The advantage of this structure is that we can use large sheets of graphene.

In Fig. 2.14, a representative GNM structure is shown. The structure consists of a single graphene sheet punched with a high-density array of nanoscale holes. We define three critical parameters such as periodicity, L_{GNM} (defined as the centre-to-centre distance between two neighbouring nanoholes), the neck width, W_n, (the smallest edge-to-edge distance between two neighbouring nanoholes), and the hole diameter, d_h. We investigate bandgap tunability by varying W_n since W_n represents the smallest dimension of the GNM and can control the charge transport of the system. We adopt the following mechanisms to vary W_n. The first mechanism is to keep d_h (8 Å) fixed

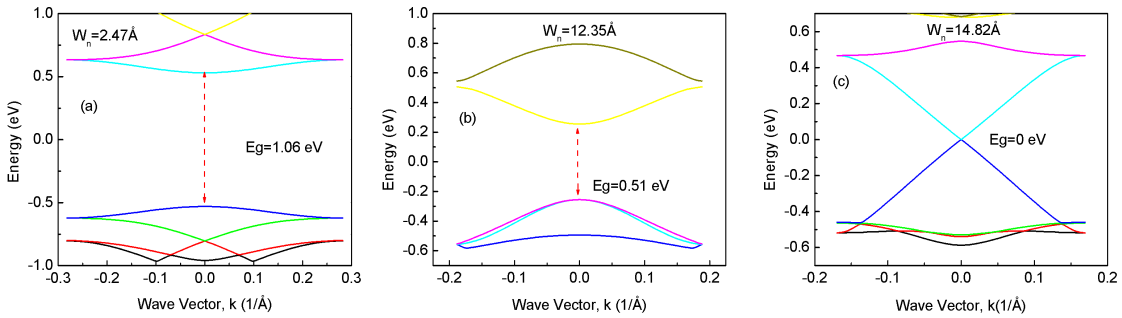

Figure 2.15: Electronic structures of GNM with (a) $W_n = 2.47$Å, (b) $W_n = 12.35$ Å and (c) $W_n = 14.82$ Å.

and vary L_{GNM} resulting in different values for W_n. The second mechanism is to vary d_h while keeping L_{GNM} fixed.

In Figure 2.15 (a-c) band structures of GNMs with varying values of L_{GNM} are presented keeping d_h fixed at 8 Å. Three different W_n values of 2.47 Å, 12.35 Å and 14.82 Å are obtained by varying L_{GNM}. For W_n= 2.47 Å, a band gap of 1.06 eV is achieved as shown in Fig. 2.15(a). The bandgadp decreases with an increase of W_n as we see in the figure. So smaller W_n and a denser mesh structure are needed to obtain a larger bandgap. As we decrease W_n (resulting in more holes per unit area) the effective mass increases. For $W_n = 14.82$ Å, the calculated bandstructure shows (Fig. 2.15(c)) the typical Dirac cone of a graphene sheet with a Fermi velocity around 4.5×10^5 m/sec.

We extend our analysis by extracting the effective mass (m^*) as shown in Figure 2.16. At W_n=12.35 Å, the obtained band gap is 0.5 eV with a m^* of $0.052m_0$. As we decrease W_n creating a denser mesh structure, both the induced bandgap and m^* increase as shown in the figure. This observation is consistent with GNR devices where the bandgap and on-off ratio are inversely proportional to the width of the ribbon. Similar to GNRs, the opening of the conduction bandgap in our GNM structure can

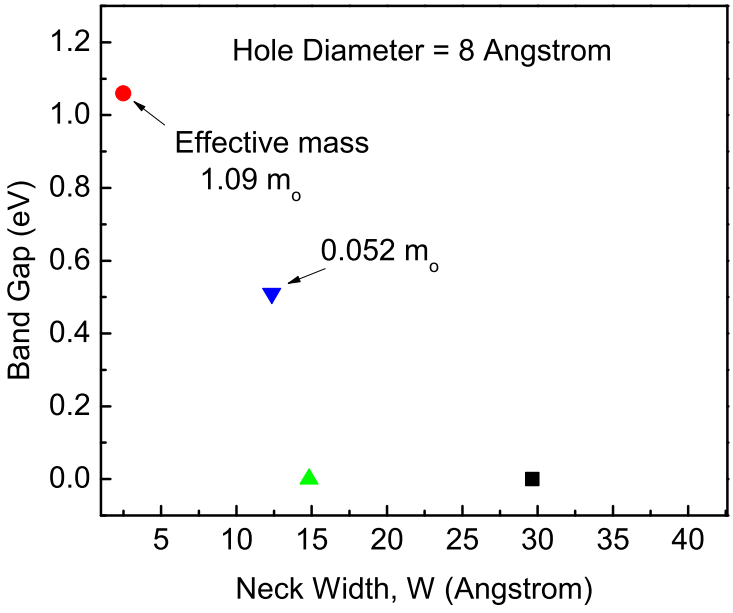

Figure 2.16: Effect on induced bandgap varying W_n using first mechanism.

be attributed to a combination of lateral quantum confinement effect [3, 81] and a localization effect resulting from edge disorder such as variable edge roughness.

Now we will discuss the effect of varying W_n on the bandstructure of a GNM. In Figure 2.17 (a-c), the calculated band structures of GNMs with different d_h are presented keeping L_{GNM} fixed at 42 Å.

We chose three different d_h values of 21.62 Å, 17.81 Å and 8.16 Å as shown in figure 2.17 (a-c), respectively. With $d_h = 21.62$ Å and $W_n = 17.29$ Å, a band gap of 0.1 eV is achieved. It is evident from the $E - k$ diagram that smaller value of W_n is needed to induce a decent bandgap. We can obtain a smaller W_n by increasing d_h while keeping L_{GNM} fixed. Therefore quantum confinement manifests itself in a GNM by W_n in either of the two approaches. The strength of the quantum confinement leading to bandgap variation is measured by W_n.

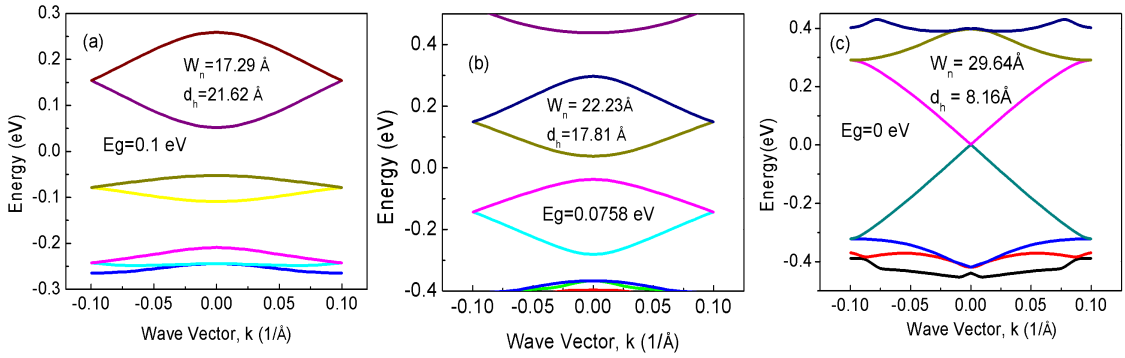

Figure 2.17: Electronic structures of GNM with different W_n by varying d_h, (a) W_n = 17.29 Å, (b) W_n = 22.23 Å, (c) W_n = 29.64 Å.

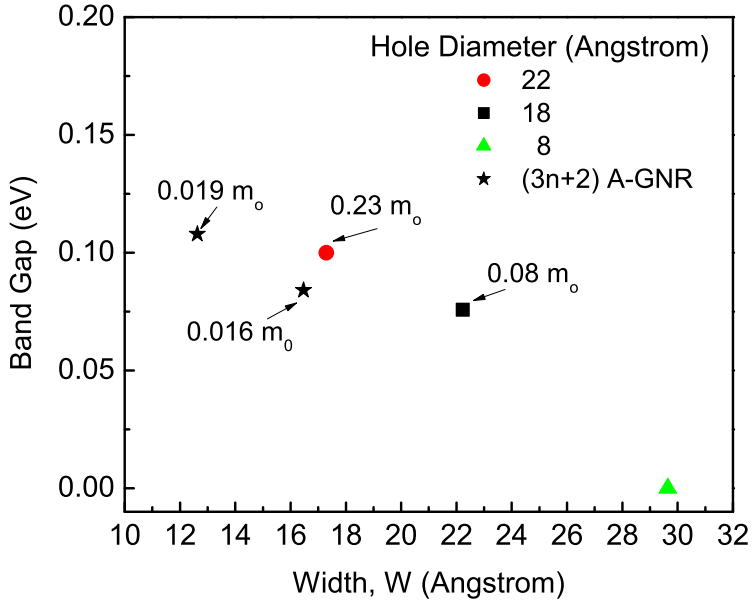

Figure 2.18: Variation of induced bandgap varying W_n using second mechanism.

Finally in Fig. 2.18, we show the band gaps and effective masses (m^*) that result from varying W_n. The calculated m^* and bandgap are also compared with that of 3n+2 AGNR discussed in section 2.2.1. The figure shows that to achieve a band gap of 0.1 eV, an AGNR of 13 Å is required. The same band gap can be achieved with a 2D GNM having a neckwidth of 22 Å.

2.3 Conclusion

In summary, we use semi-empirical extended Huckel theory and NEGF to investigate the dispersion relation of graphene based structures. Significant bandgap opening is observed in all proposed structures. We found that dangling bonds at the unpassivated edges of an AGNR create extra modes in the channel region, and that they are removed by H passivation. The magnitude of effective mass is inversely proportional to the width of the AGNR. External bias has a significant effect on the bandstructure of bilayer GNRs. Based on this property we considered a device of two stacked monolayers of AGNR termed a s-AGNR device. The stacked device shows negative differential resistance (NDR) behavior. The magnitude of the NDR decreases with increased ribbon width. Finally, we study the method of tuning bandgap in a GNM consisting of uniformly distributed holes in a 2D graphene sheet. The bandgap is governed by the spacing between the holes, and a spacing of 22 Å results in a bandgap of about 0.1 eV.

Chapter 3

Gate Induced Negative Differential Resistance in Graphene Field-Effect Transistors

3.1 Introduction

Graphene field-effect transistors (GFETs) could be useful in analog and radio frequency applications where high ON/OFF current ratios are not required. Graphene does not have an energy band-gap, a serious hurdle for its applications in digital logic gates. The efforts to induce a band-gap in graphene via quantum confinement or surface functionalization have not resulted in a breakthrough. Motivated by recent studies [86,87] on the use of GFETs for new concepts of electronic devices, we carried out further investigation of the nonlinear behavior of a GFET. Our theoretical investigations, confirm an unconventional biasing approach that results in negative differential resistance (NDR) in single layer and bilayer GFETs. An atomistic model based on the Extended Huckel Theory (EHT) coupled with the non-equilibrium Green's

function formalism (NEGF) is used for electronic transport calculations. The calculated current-voltage characteristics of single layer and bilayer GFETs show NDR behavior at room temperature which originates from the symmetric band structure of graphene. The theoretically calculated NDR in a GFET of conventional design is supported by experimental investigations. The atomistic modeling shows that the negative differential resistance appears not only in the drift-diffusion regime but also in the ballistic regime at the nanometer-scale although the physics changes.

3.2 Device Structure and Biasing Scheme

A representative schematic diagram of a device is shown in Fig. 3.1. The device consists of a single layer or bilayer graphene sheet as a conducting channel for the SLGFET or BLGFET, respectively. For the BLGFET, two single-layer graphene sheets are stacked in AB alignment with a separation distance of 3.35 Å. The dielectric material for both the SLGFET and BLGFET on top of the channel is a high K dielectric. The left and right contacts are single-layer graphene for the SLGFET and bi-layer graphene for the BLGFET. The total channel length between the two leads is 30nm for both the SLGFET and the BLGFET. In the conventional biasing scheme of a GFET [88–90], only one terminal is varied while the rest are fixed. Here, we use two types of unconventional biasing schemes for both the SLGFET and the BLGFET. In the first biasing scheme, the gate voltage V_{TG} is varied from negative to positive voltage while the source-drain voltage V_{DS} is simultaneously increased from 0 to positive voltage. The gate voltage is swept faster than the drain voltage. The second biasing scheme is a diode-connected configuration in which the gate and drain are shorted.

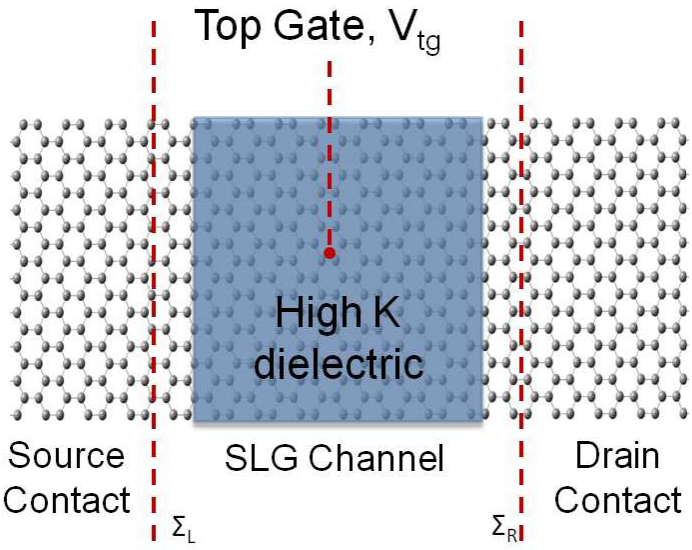

Figure 3.1: Schematic diagram of the single layer graphene device with the contact surface self-energies. The region inside the vertical lines is the channel region.

3.3 Results and Discussion

The experimental device shown in Ref. [1] is large and operates in the drift-diffusion regime. However, for future applications one has to consider electron transport in scaled devices with feature sizes on the order of a few nanometers. Here, we perform a theoretical analysis of a nano scaled GFET that operates in the ballistic regime. In Figure 3.2, the simulated $I - V$ characteristics of a SLGFET with two different Fermi levels are presented for the first biasing scheme where we sweep top gate voltage (V_{TG}) from -8 V to 8 V while changing drain to source voltage (V_{DS}) from 0 to 0.1 V simultaneously. The back gate (V_{BG}) voltage values corresponding to the Fermi levels are taken from the experimental setup [1] and are listed in Figure 3.2. From the experimentally [1] obtained transfer characteristics ($I_D - V_{TG}$), we extract the minimum point that corresponds to the charge neutrality point. To calculate the potential in the channel region we use a capacitance model [91] combined with the numerically calculated density of states . On top of the channel, an Al_2O_3 layer of 23 nm is taken as dielectric material of the SLGFET. The larger the top-gate capacitance, the smaller the sweep range of V_{TG} is required. For our gate oxide we use V_{TG} within the range of values that are several times larger than those of V_{DS}. In the case of the BLGFET, the dielectric layer thickness is taken as 12nm (2nm Al_2O_3 and 10nm HfO_2). The dielectric layer thickness is chosen from experimental study. The calculated $I - V$ characteristic shows NDR characteristics which qualitatively follow the experimental trend [1]. The current valley position occurs at a lower bias region for heavily doped n type devices.

The transport mechanism responsible for the NDR effect can be explained through $E - k$ relationships and the transmission curves shown in Figure 3.3 and 3.4 respectively. Figure 3.3(i) shows the line-up of the bands in the source, channel, and drain

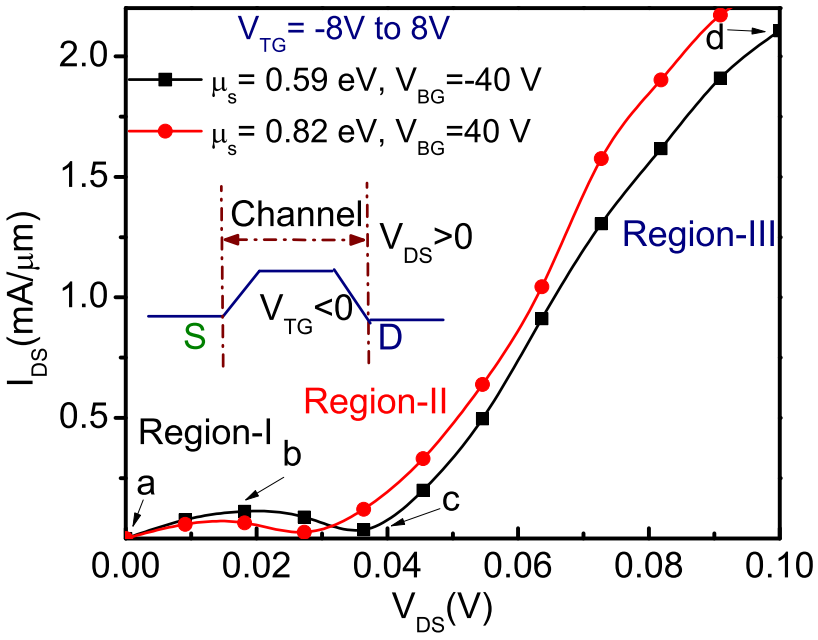

Figure 3.2: I-V characteristics of a n-type SLGFET with different Fermi energies (μ_s). (inset: schematic diagram of the energy profile in the SLGFET channel region for $V_{TG} < 0$, $V_{DS} > 0$)

regions in equilibrium. Figure 3.3(ii) shows the line-up of the bands in region-I of the $I-V$ curve (between points a and b) of Fig. 3.2. In this region, the source is grounded. The drain voltage is positive. The channel potential is negative. The result, going from source to drain, is an n-p-n junction. The source conduction band (SCB) overlaps with the channel valence band (CVB). Under a small drain bias the electrons transition from SCB to CVB. With increasing drain voltage, current increases as long as the source conduction band and channel valence band overlap within the transport window between μ_s and μ_d. After the peak current at point 'b' of the $I-V$, the overlap area of the source conduction band and channel valence band starts diminishing with increasing V_{TG}. It reaches a minimum as shown in Fig. 3.3(iii) at the valley current at point 'c' of the $I-V$ curve. With further increase of V_{TG}, the channel region becomes n-type as shown in Figure 3.3 (iv). and the transport takes place through unipolar junctions. As a result, current again starts increasing with increasing V_{TG} and V_{DS} as seen in region III of figure 3.2 .

In order to further elucidate the origin of the observed NDR effect, we calculated the transmission coefficient shown in Figure 3.4 as a function of the energy. The Fermi level of the source contact (μ_s) remains constant whereas the drain Fermi level (μ_d) shifts with V_{DS}. As V_{TG} varies from negative to positive voltage, the Dirac point shifts from the higher to lower energy. The current at any bias is proportional to the area under the transmission curve bounded by the Fermi levels (μ_s-μ_d). Figure 3.4 shows the drain Fermi level for three different cases marked as μ_{d1}, μ_{d2} and μ_{d3}. At bias μ_{d2}, the Dirac point is within the energy window (μ_s- μ_{d2}), and the transmission is suppressed. The density of states (DOS) at the Dirac point is a minimum, and the probability of electron transmission from left to right lead is also minimum leading to a valley current. The maximum transmission region is obtained when ectron states and hole states match in the contact and channel regions resulting in the peak current.

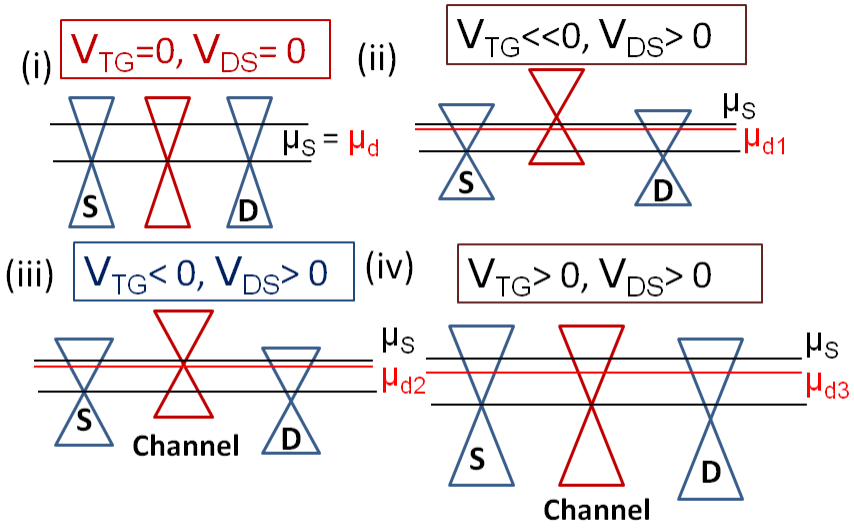

Figure 3.3: Schematic illustration of energy spectrum of SLGFET showing source, drain and channel region (i) no bias condition (ii) n-p-n junction (iii) minimum conduction near CNP (iv) unipolar junction

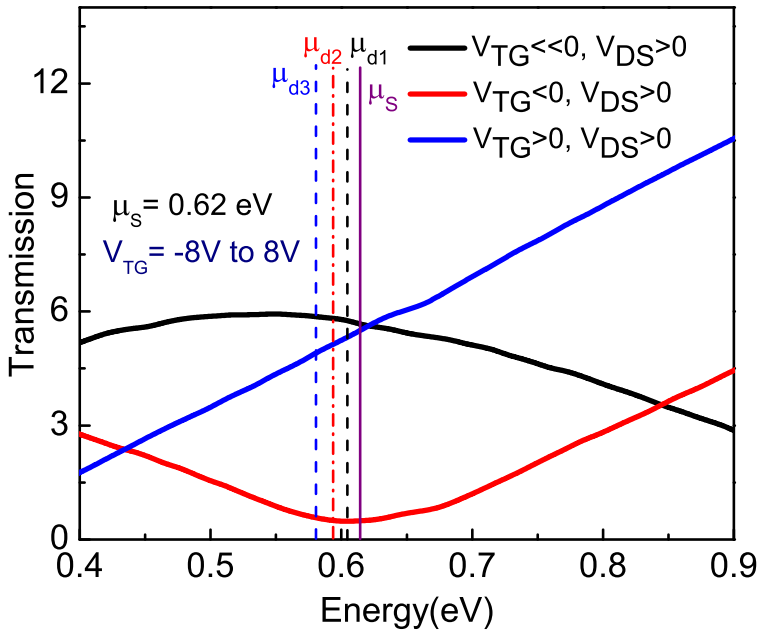

Figure 3.4: Transmission coefficient of SLGFET as a function of energy for different values of V_{TG} and V_{DS}. μ_s is the Fermi level for the source and μ_{d1}, μ_{d2} and μ_{d3} are the Fermi level for drain contact with different drain voltage V_{DS}.

Now we turn to our analysis to the BLGFETs following a similar biasing scheme where V_{TG} is swept from -3 V to 0 V and V_{DS} from 0 to 0.1 V. The flat band energy profile in the channel region is shown in Figure 3.5. The top gate oxide for this device is 12 nm (2 nm Al_2O_3/10 nm HfO_2). For the BLGFET, the back gate oxide (d_{BG}) is taken as 300 nm thick SiO_2. We calculate the voltage drop using a capacitance model (see inset of fig. 3.11) as shown below:

$$U_2 = U_1 \frac{C_{12}}{(C_{12} + C_{TG2})} \tag{3.1}$$

where U_2 and U_1 is the potential of the top and bottom layer of bilayer graphene

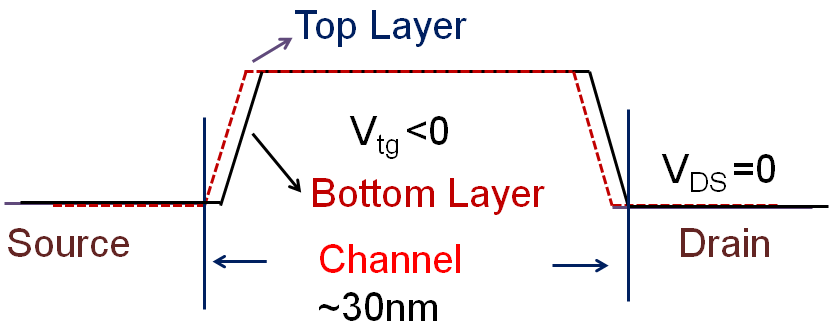

Figure 3.5: Schematic diagram of the energy profile in the BLGFET channel region for $V_{TG} < 0$, $V_{DS} = 0$.

sheet respectively, C_{TG2} and C_{12} is the back gate oxide capacitance and capacitance between the bilayer graphene sheet respectively. Since $d_{12} << d_{BG}$, $C_{TG2} << C_{12}$. Therefore, $U_2 = U_1$. Since both the layers have the same potential, the bandgap of bilayer graphene channel is zero. The potential in the channel region is calcualted similar to that of the SLGFET.

The simulated $I - V$ characteristics curve of the BLGFET is shown in Figure 3.6. Here, the Fermi energy is selected from the experimental data. The curves qualitatively follow the curves of the experimental data. The maximum peak to valley ratio is about 3-5 depending on Fermi position and bias level. The calculated NDR ratio also agrees well with that of experimental data [1].

Next we theoretically analyze a highly scaled version of the GFET in a diode connected configuration (i.e., the second biasing scheme). The device is considered to

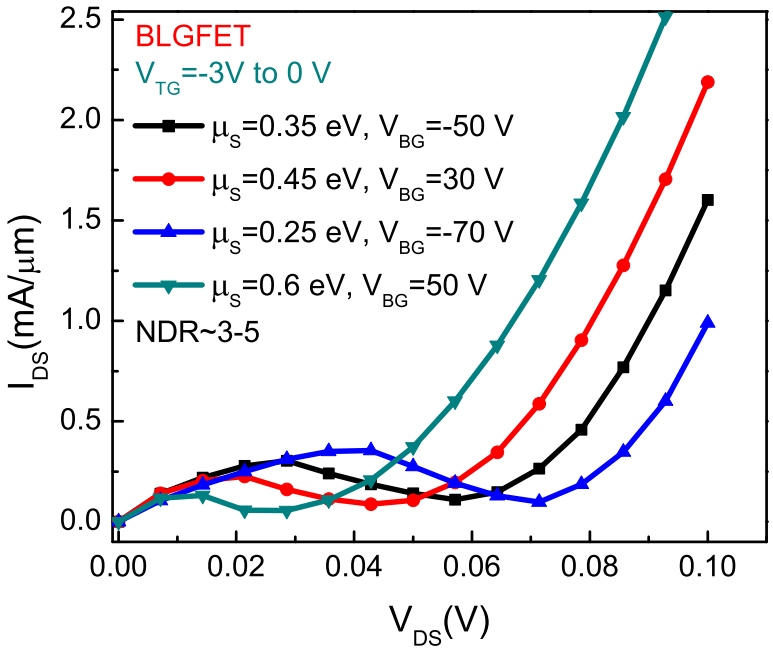

Figure 3.6: $I - V$ characteristics of top gated BLGFET with different Fermi energy (μ_s)

operate in the ballistic, quantum-capacitance limit and we determine whether such a FET, in the diode-connected configuration, will have a current-voltage response exhibiting NDR. To investigate transport properties in the quantum capacitance regime, we consider a 3 nm gate oxide with a dielectric constant of 25. The calculated gate oxide capacitance C_G is 7.3 $\mu F/cm^2$. The device is in the quantum capacitance regime when $C_G > C_Q$ where C_Q is the quantum capacitance of the channel [91]. In equilibrium, the source-to-drain potential profile is that of an npn structure in which the source and drain are n-type and at the same potential, and the channel is p-type. The built in potential (V_{pn}) between the source and the channel region as shown in Fig. 3.7 (inset) is $V_{pn} = 2\mu_s$ where μ_s is measured from the charge-neutral point of the source. The current-voltage response shown in Figure 3.7 is calculated for a diode-connected SLGFET, i.e. the gate is shorted to the drain. The $I - V$ response does exhibit NDR, and for a higher value of μ_s, the peak to valley current ratio increases. The $I - V$ response demonstrates NDR for an effective 22 nm channel operating in the ballistic limit and the quantum capacitance regime.

This regime is the opposite of the diffusive regime of the experimental device [1]. Although the transport physics is qualitatively different, the physical mechanism governing the NDR is qualitatively the same. NDR results when the Dirac cone in the channel can be moved sufficiently fast with respect to the gate voltage in the drain. In a diode connected GFET in the quantum capacitance regime, this ration is 1:1. The origin of the NDR behavior of the ballistic device can be described by the transmission curves shown in figure 3.8 and the corresponding band alignments shown in the insets. At low bias, the transmission is given by the red curve corresponding to the band-alignment shown in the left inset. The transmission is limited by the transition between the source conduction band and the channel valence band. Conservation of energy and momentum cause the transmission to be proportional to the area of the

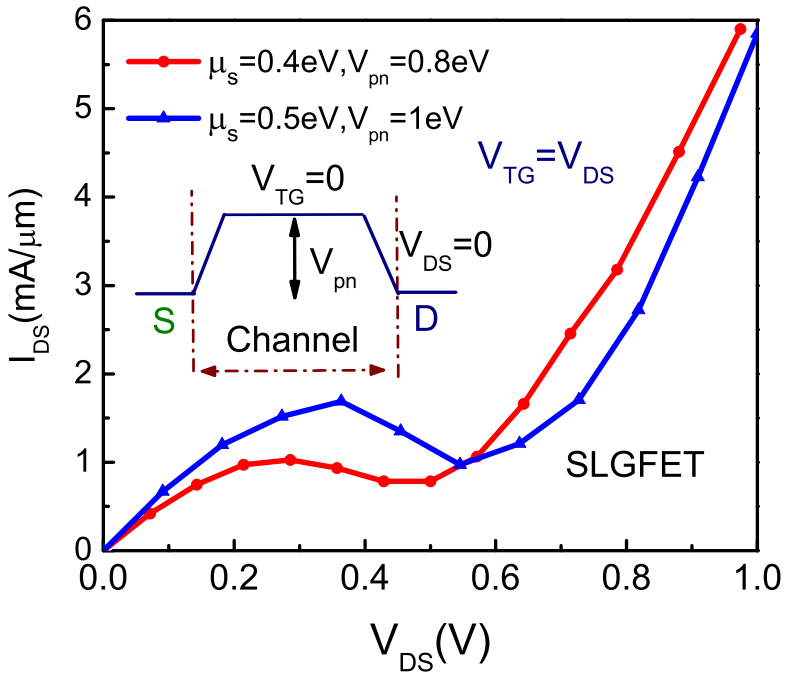

Figure 3.7: $I-V$ characteristics for different Fermi energy keeping $V_{pn} = 2\mu_s$. (inset: flat band profile of the device.)

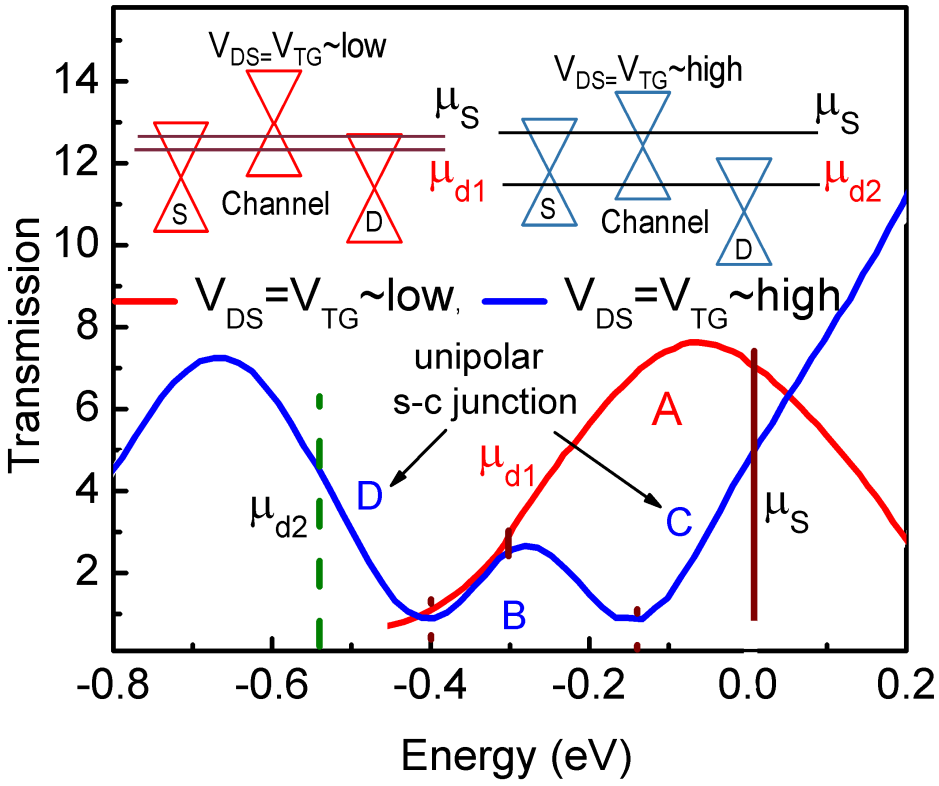

Figure 3.8: Energy spectrum of drain-gate shorted SLGFET for low and high bias region (inset). Transmission coefficients as a function of energy. The Transmission plot corresponds to the minimum and maximum current of fig. 3.7 ($\mu_s = 0.5$ eV) where μ_s is the fermi level of the source and μ_{d1} and μ_{d2} are the fermi levels of drain contact at maximum and minimum current respectively.

overlapping inverted triangles representing the electron and hole dispersions. The minimums in the red transmission curve correspond to the energies of the charge neutral points in the source and the channel. The current is proportional to the area under the transmission curve between the source Fermi level (μ_s) and the drain Fermi level (μ_{d1}) shown on the transmission plot. As the bias turns on, this area initially increases and the current increases.

As the bias continues to increase, the charge-neutral point of the channel is pulled down into the energy window between the source and drain Fermi levels as shown in the right inset of figure 3.8 resulting in the blue transmission curve. The two

minimums in the transmission again correspond to the charge neutral points that have now been brought closer together in energy. The transmission regions labeled D and C result from unipolar transport between the source and channel, hole-hole and electron-electron, respectively. The region labeled B lying between the two charge-neutral points results from interband transport between the source conduction band and the channel valence band. The minimum in transmission at negative energies outside of the domain of the graph results from the charge-neutral point of the drain. At this bias, even though the difference between the source and drain Fermi levels, μ_s and μ_{d2}, has increased, the area under the transmission curve is a minimum, resulting in the current minimum and NDR.

In order to extend our analysis further we also simulate $I-V$ characteristics (see figure 3.9) for other cases such as $V_{pn} > 2\mu_s$ and $V_{pn} < 2\mu_s$ and observe that NDR behavior is less pronounced. This is because the contribution of region 'A' at low bias becomes less dominant than that of other two regions 'C' and 'D' at high bias as shown in Figure. Therefore for the second biasing scheme the maximum NDR, keeping fixed Fermi energy is obtained when built in potential, $V_{pn} = 2\mu_s$.

Now we turn to our analysis to the diode connected BLGFET. We follow the biasing scheme described in the previous section. To calculate the voltage between the graphene layers we use two different approaches. In the first approach, we consider no bandgap and in the second approach, a bandgap is induced. In our first approach, a 3nm dual high-K, top and bottom gate are required to keep the BLGFET in the quantum capacitance limit. The gates are shorted, so that the two layers of the bilayer are at equal potential. In this case, the gate bias induces no bandgap in the bilayer graphene, since no potential difference is created between the layers. The current-voltage response of the diode-connected bilayer G-FET (BLGFET) is similar to that of the SLGFET. A comparison of the SLGFET and the BLGFET with the

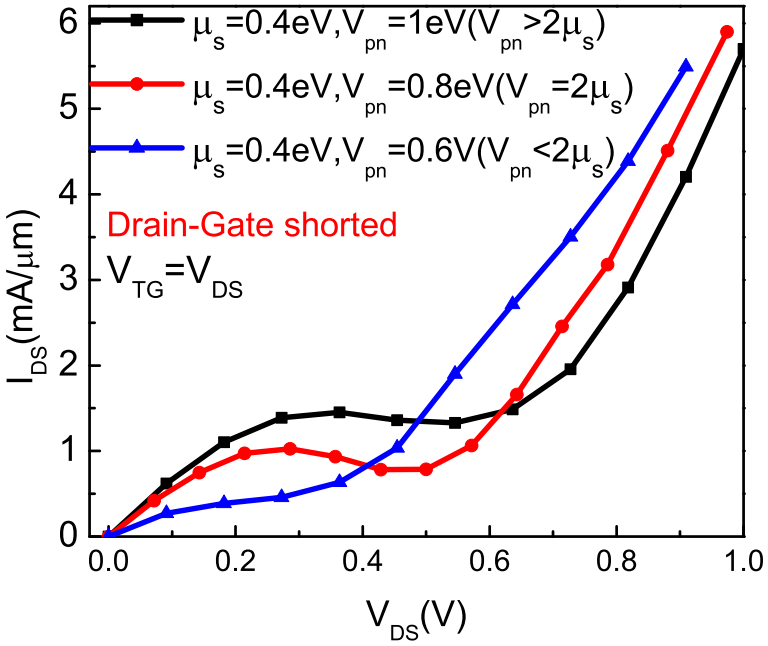

Figure 3.9: $I - V$ characteristics plotted for drain-gate shorted SLGFET at fixed fermi energy and different V_{pn}.

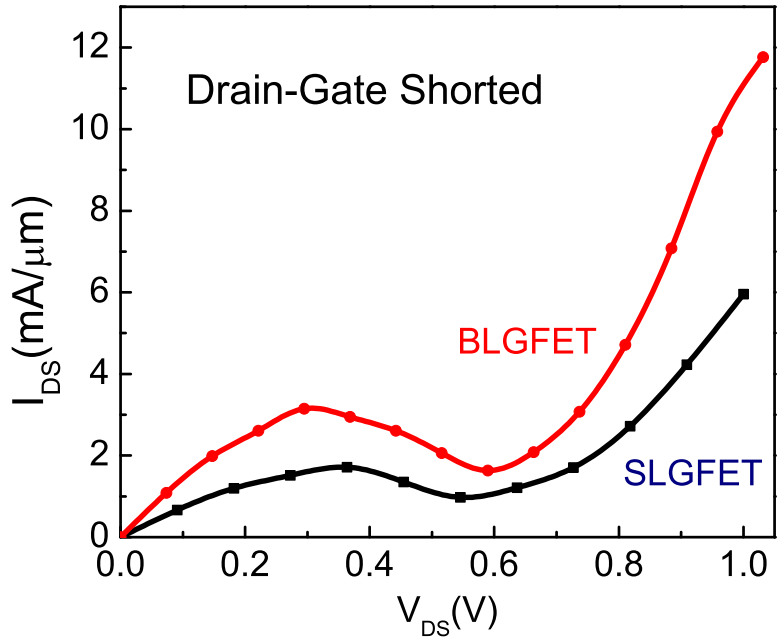

Figure 3.10: Comparison of simulated $I-V$ characteristics of SLGFET and BLGFET. Current plotted for μ_s =0.5eV and a built in potential of 1eV

same Fermi levels and built in potentials is shown in figure 3.10. The peak-to-valley current ratio of 2.0 for the BLGFET is slightly greater than the PVCR of 1.8 for the SLGFET. The analysis of the transmission for the BLGFET is similar to that of the SLGFET. Although the density of states is finite at the charge neutral point, it is still a minimum, and the transmission curves look qualitatively the same as in figure 3.8.

In our second approach, we consider 3 nm high-k symmetric top and back gate oxides with V_{BG} =0. Such a configuration is required to create a potential difference between the two graphene sheets. The schematic capacitor model used for calculating the potential difference between the layers of the bilayer graphene device is shown in Fig. 3.11 (inset).

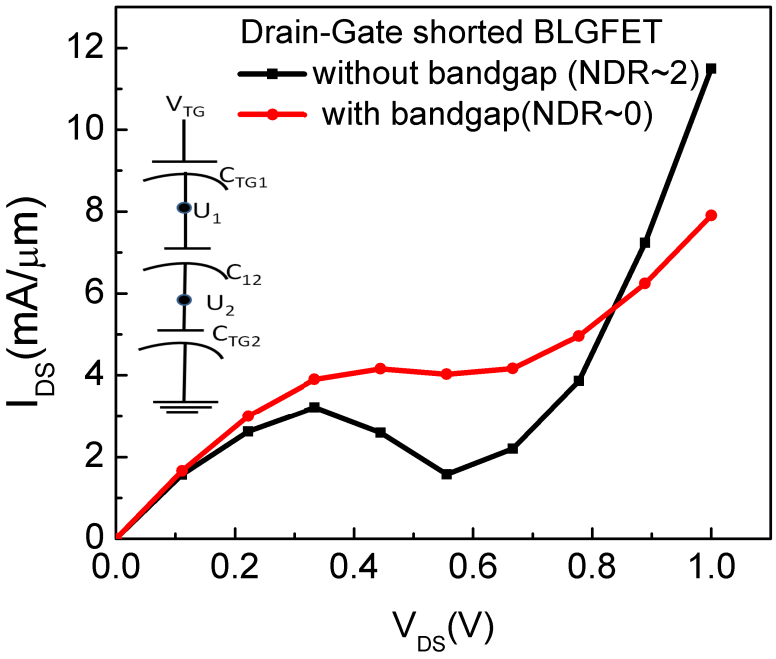

Figure 3.11: Comparison of $I-V$ characteristics of bilayer drain gate shorted device. Current plotted for $\mu_s = 0.5eV$ and a built in potential of 1 eV, (inset: Schematic diagram shows the gate oxides capacitance (C_{TG1}, C_{TG2}) and capacitance C_{12} in between the bilayer graphene sheet).

The thickness of both the top and the bottom gate oxide is taken as 3 nm high-k which results in $C_{TG1} = C_{TG2} \approx C_{12}$. Considering an interlayer distance between the top and bottom layer $d_{12} = 3.35$Å, $C_{12} = 2.643\mu F/cm^2$. Therefore we get

$$U_2 = V_{TG}\frac{C_{TG1}^{-1}}{\left(C_{12}^{-1} + C_{TG2}^{-1} + C_{TG1}^{-1}\right)} \tag{3.2}$$

$$U_1 = V_{TG}\frac{C_{TG1}^{-1} + C_{12}^{-1}}{\left(C_{12}^{-1} + C_{TG2}^{-1} + C_{TG1}^{-1}\right)} \tag{3.3}$$

As $C_{TG1} = C_{TG2} \approx C_{12}$, we get $U_2 = \frac{1}{3}V_{TG}$ and $U_1 = \frac{2}{3}V_{TG}$. Therefore the voltage drop in between the layers is $\frac{1}{3}V_{TG}$, and the *average* voltage drop of the layers is $V_{TG}/2$. This is simply the average of the symmetric top and back gates with one at V_{TG} and one at ground. To create the maximum potential difference between the two graphene sheets, one must sacrifice half of the potential control of the channel.

We calculate the $I - V$ characteristics of the BLGFET device for both of these approaches and show the comparison in Fig. 3.11 for $\mu_F = 0.5$eV and V_{pn}=1eV. We can see that in case of bilayer graphene with symmetric gates, even though a bandgap is induced, the NDR is lost. The loss of NDR results from the loss of gate control of the average channel potential.

3.4 Conclusions

Using the EHT and NEGF technique, we have investigated the transport characteristics of nano-scaled SLGFETs and BLGFETs at room temperature. NDR appears in both of the devices. To create a maximum potential difference between the two graphene sheets of a BLGFET, one must sacrifice half of the potential control of the channel. The benefit of inducing a bandgap with gate voltage is outweighed by the

cost of losing half of the potential control of the channel. The net result is a reduction in the magnitude of the NDR. The peak-to-valley difference increases for increasing doping concentration of graphene sheets.

Chapter 4

Interlayer magnetoconductance of misoriented bilayer graphene ribbons

The coherent, interlayer conductance of misoriented bilayer graphene ribbons is a strong function of the Fermi energy,magnetic field and temperature. Edge states can result in a large peak in the interlayer transmission at the charge neutrality point that is several orders of magnitude larger than the surrounding low-energy transmission. The coherent interlayer conductance is consistently asymmetric around the charge neutrality point for all structures with the value differing by up to 3 orders of magnitude at $E_f = \pm 0.05$ eV. The low-energy states exhibit a high magnetoconductance ratio, and the magnetoconductance ratio tends to increase as the width of the ribbons decrease. The maximum value for the 35 nm wide bilayer ribbons at 10T is 15,000%. Non-equilibrium Green's function calculations of the interlayer transport properties are also supported by semi-analytical calculations based on Fermi's Golden Rule. This intrinsic magnetoconductance effect is realized without the use of any ferromag-

netic leads and can be promising for future spintronics applications. We also study interlayer bias dependency on simulated interlayer conductance. The nature of the bias modulated conductance gives rise to non-linear current-voltage characteristics.

4.1 Introduction

The electronic structure of bilayer graphene is highly sensitive to the stacking geometry [15, 16]. Experimentally, the layers of bilayer or multilayer graphene tend to be rotated (i.e., twisted or misoriented) with respect to each other. [45–47] The need to understand the electronic properties of twisted graphene layers stimulated a number of theoretical and experimental investigations. [11,46–53,92–95] The low energy states in each layer of misoriented bilayer graphene are effectively decoupled and maintain a linear dispersion for twist angles greater than a few degrees. Turbostratic graphitic structures maintain the high mobility of graphene. [96] The electronic decoupling and high interlayer resistance is a coherent quantum effect resulting from destructive interference between the electron wavefunctions of the two rotated layers. [50]

The coherent interlayer transmission is a strong function of the twist angle, and it can be strongly suppressed giving high interlayer contact resistances. [56] Bistritzer and MacDonald found coherent interlayer contact resistances changing by 16 orders of magnitude as the rotation angle is changed by 30°. [56] Resistances values varied from 10^{15} $\Omega\mu\text{m}^2$ to 0.1 $\Omega\mu\text{m}^2$. Recent calculations of the phonon-mediated, interlayer conductance indicate that the phonon-mediated current is a significant interlayer transport mechanism at room temperature. [57] The phonon-mediated current has a weaker dependence on rotation angle. At room temperature with a Fermi level 260 meV above the Dirac point, the interlayer resistance was found to smoothly vary from 50 $\Omega\mu\text{m}^2$ at small rotation angles of a few degrees to 330 $\Omega\mu\text{m}^2$ at a rotation angle

of 30° [57]. Experimental measurements found similar trends but a higher resistance that varied from 750 $\Omega\mu m^2$ to 3400 $\Omega\mu m^2$ [97].

The coherent electronic decoupling between two dimensional rotated graphene sheets is still present when the overlap region is scaled to a few nanometers [11]. Two armchair nanoribbons overlapping at an angle of 90° result in a misoriented overlap region with a crystallographic rotation angle of 30°. Even with an overlap region of 1.8 nm × 1.8 nm, the coherent interlayer transmission is reduced by approximately 5 orders of magnitude. In such structures, an interlayer voltage can result in a large modulation ($\sim 10^3$) of the coherent interlayer current [11]. The vibrational modes and their effect on the current of the crossed GNR system have not yet been investigated.

In addition to electronic properties, the unique chiral nature of quasi-particles in graphene results in a novel quantum Hall effect [17–19] that opens a new possibility for spintronic applications [58, 59]. The integer quantum Hall effect in bilayer graphene indicates the presence of massive chiral quasiparticles [98] with a parabolic dispersion at low energy. The electron motion in twisted graphene is modulated by the application of an external perpendicular magnetic field (B-field). The B-field introduces the Peierls phase in the Bloch functions and thus modifies the energy-momentum dispersion, the subband spacings, the energy width, and the local density of states [82, 99, 100]. At sufficiently large magnetic field, the cyclotron diameter of the electron motion becomes smaller than the GNR width, resulting in the formation of Landau levels [60, 82].

GNRs can have interesting magneto-electronic properties with high magnetoresistance. [58, 63, 65, 66] GNRs with zigzag edges (ZGNRs) have shown magnetism both theoretically [58, 101, 102] and experimentally [103]. A spin-valve device based on a graphene nanoribbon has been reported where the magnetoresistance is configured with two ferromagnetic (FM) states of ZGNR electrodes (parallel vs. antiparallel

alignments) and the results of first-principles simulations exhibit high magnetoresistance values [58]. Saffarzadeh and Asl [66] investigated spin polarized transport of the planar FM/Grahene flake/FM junction with zigzag interfaces and showed that the junction exhibits a spin valve effect with magnetoresistance ratios as high as 95%. Experimentally a 10% magnetoresistance ratio in a GNR based spin valve device has been observed, where a 200 nm GNR was connected to NiFe contacts [62]. Another experimental study reported a negative magnetoresistance of nearly 100% at low temperatures, and over 50% at room temperature [63]. Hwang and Sarma [68] predicted a negative magnetoresistance for intrinsic graphene and a nonmonotonic magnetoresistance for extrinsic graphene with a parallel magnetic field. In most of the previous studies, a magnetoresistance effect was induced by a change in the relative magnetic orientations of FM contacts.

In addition to the above intrinsic properties, novel van der waals (vdW) heterostacks of graphene and non-graphene layers (MoS_2, hBN, Bi_2Te_3, TiO_2 etc.) have been demonstrated. [41, 104–114] Several types of heterostructures consisting vdW materials have been proposed for various applications such as high mobility electronic devices [104], molecular scale electronic devices [105], nonvolatile memory cells [108] and magnetic field effect transistors [109]. The fabrication approach often consists of creating various individual materials by exfoliation and/or growth followed by mechanical stacking [111]. Such a procedure naturally leads to misoriented interfaces.

The coherent interplane transport between misoriented graphene layers is governed by quantum interference and the relative phases of the wavefunctions of the two layers. Since magnetic fields modify the phase of the electronic wavefunction, one might expect that the interlayer transport could be sensitive to an applied magnetic field. Any real structure is finite in size. It has edges where localized edge states can exist. If the scaling laws for heterostructure bipolar transistors serve as a guide,

the horizontal dimensions of devices proposed to attain THz cutoff frequencies must be on the order of tens of nanometers [115]. For these reasons, we investigate the interlayer transport between two stacked graphene ribbons with a crystallographic misorientation of 30°. Such a geometry results from an armchair ribbon on a zigzag ribbon. The widths of the nanoribbons considered range from 35 nm to 70 nm. The interlayer magnetoconductance is calculated as a function of Fermi level and perpendicular magnetic field. The magnetic field variation of the interlayer conductance can be large, changing by several orders of magnitude.

4.2 Method

A numerical approach and a semi-analytical approach are used to give insight into the interlayer coupling. The band structure calculations are performed using a tight binding π-bond model. The electron transmission and conductance are calculated using the non-equilibrium Green's function (NEGF) formalism. The interlayer transmission is also calculated semi-analytically using Fermi's golden rule and compared with NEGF results. The calculation methods and the device structure are discussed below.

4.2.1 Misoriented bilayer structures

Figure 4.1(a,b) shows the schematic structure of the four-terminal misoriented bilayer graphene nanoribbon (mBGNR). It consists of two graphene nanoribbons (GNRs), an armchair nanoribbon (AGNR) placed on top of a zigzag nanoribbon (ZGNR) with a vertical separation of 3.35Å . The alignment of the two GNRs corresponds to a crystallographic misorientation angle of 30°. A 30° rotation is an incommensurate rotation angle, [50] so that there is no periodicity in the bilayer structure. The top view

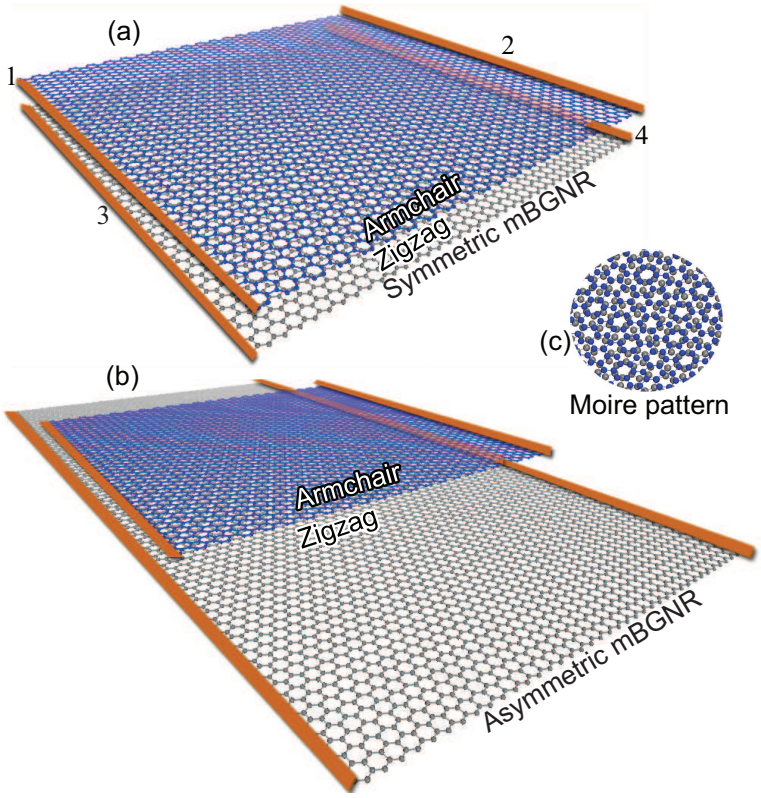

Figure 4.1: Schematic diagram of mBGNR, highlighted region shows the Moire pattern within the overlapped channel region.

of a section of the bilayer shown in Fig. 4.1(c) displays the Moire pattern resulting from the two misoriented graphene layers. Two types of mBGNRs are considered, symmetric structures in which both GNRs have the same width as shown in Fig. 4.1(a) and asymmetric structures in which the AGNR is narrower than the ZGNR as shown in Fig. 4.1(b). The asymmetric structures serve to move the overlap region away from the zigzag edges which dominate the low-energy interlayer transmission.

The contact regions denoted by the gold termination at the ends of the nanoribbons are treated as semi-infinite continuations of the the individual armchair or zigzag ribbon with no interlayer coupling. Physically, such a system would be implemented using a thin insulator such as BN with a window etched out. In the area of the window, the graphene layers would be in intimate contact. The contacts would be

made outside of the window to the individual layers separated by the insulator.

4.2.2 Numerical model

The interlayer transport of the mBGNR is calculated using a tight-binding (TB) Hamiltonian with the NEGF formalism [116, 117] in the presence of an external perpendicular magnetic field. The intralayer nearest-neighbor hopping parameter is $\gamma_0 = 3.16$ eV. The interlayer hopping between atom i on the top layer and atom j on the bottom layer is calculated using $\gamma_{ij} = \gamma_1 e^{-3(d_{ij}-d_0)}$ where d_{ij} is the distance between atom i and atom j, $\gamma_1 = 0.39$ eV is the interlayer nearest neighbor hopping and $d_0 = 3.35$Å is the inter-GNR distance. [118] The inplane cutoff distance is $3a_{cc}$, where a_{cc} is the C-C bond length. The applied perpendicular B-field of $\mathbf{B} = (0, 0, B_z)$ induces a vector potential $\mathbf{A} = (-B_z y, 0, 0)$. In the presence of an external perpendicular magnetic field, the coupling energy between neighboring atoms acquires a Peierls phase factor. [119] The coupling $\gamma_{0(1)}$ is modified to $\gamma_{0(1)} \exp(iq \int_{l_m}^{l_n} \mathbf{A} \cdot d\mathbf{l}/\hbar)$, where $l_{n(m)}$ is the coordinate of atom n(m). The magnetic field is included in both the channel and the contact regions.

To compute the interlayer transmission $T(E)$ of such large aperiodic structures, the channel region is divided into $4a_{cc}$ wide blocks. Each block consists of a different number of atoms due to the non periodicity. The Hamiltonian matrix elements of these nonuniform blocks are used in a non-uniform recursive Green's function (RGF) algorithm to calculate the Green's function of the channel as described in Ref. [[120]]. In the contact region, γ_1 is set to zero so that the 4 contacts are isolated from each other. The self energies of the four contacts are calculated with the decimation method [121] using a 1 meV convergence factor. The transmission between a left contact on the top GNR and a right contact on the bottom GNR, $T(E)$, is calculated

from the standard Green's function expression,

$$T(E) = \mathrm{tr}\{\Gamma^a_{1,1} G^R_{1,N} \Gamma^z_{N,N} (G^R_{1,N})^\dagger\} \tag{4.1}$$

where the indices 1 and N indicate the first and last block-layers of the mBGNR channel, respectively. Denoting the armchair contact self-energy on the left as $\Sigma^a_{1,1}$ and the zigzag contact self-energy on the right as $\Sigma^z_{N,N}$, then the injection matrices Γ in Eq. (4.1) are given by $\Gamma^a_{1,1} = i(\Sigma^a_{1,1} - \Sigma^{a\dagger}_{1,1})$ and $\Gamma^z_{N,N} = i(\Sigma^z_{N,N} - \Sigma^{z\dagger}_{N,N})$. The zero-temperature conductance G is given by,

$$G = \frac{e^2}{\hbar} T(E_F). \tag{4.2}$$

where E_F is the Fermi level. The magnetoconductance (MC) ratio is,

$$MC \equiv \frac{G(B) - G_0}{G_0} \tag{4.3}$$

where $G(B)$ and G_0 are the conductance at a specific Fermi energy calculated at finite magnetic field and zero magnetic field, respectively. The diagonal elements of the spectral function, $A_{i,i}(E) = -2\mathrm{Im}G^R_{i,i}(E)$, where i is the atom index, will be plotted to give insight into the spatial overlap of the wavefunctions on the two GNRs.

4.2.3 Analytical Model

The analytical expression for $T(E)$ obtained from Fermi's golden rule is [11],

$$T(E) = 4\pi^2 \sum_{m,n} |M_{m,n}|^2 N^n_a(E) N^m_z(E). \tag{4.4}$$

The matrix element $M_{m,n}$ is calculated between a k_a state of mode n on the AGNR and a k_z state of mode m on the ZGNR. $N_a^n(E)$ and $N_z^m(E)$ are the 1D density of states of the armchair and zigzag nanoribbon, respectively. $T(E)$ depends on both the magnitude of the matrix element squared between the electron wavefunctions of the top and the bottom layer and the joint density of states of the two GNRs. The matrix element $M_{m,n}$ is calculated using the electronic wave functions of the isolated GNRs and expressed as,

$$M_{m,n} \equiv \langle \psi_{m,k_z} | H_{\text{int}} | \psi_{n,k_a} \rangle \tag{4.5}$$

where $|\psi_{m,k_a}\rangle$ and $|\psi_{n,k_z}\rangle$ are the Bloch wavefunctions for the armchair and the zigzag nanoribbons, respectively, and H_{int} is the interlayer component of the tight-binding Hamiltonian. The Bloch wavefunctions for the isolated armchair and zigzag nanoribbons are the eigenvectors of the tight-binding Hamiltonian H_k for each nanoribbon. The wavefunctions are extended over multiple unit cells of the nanoribbons using Bloch's theorem, $\psi_{m,k}(na) = e^{iknа}\psi_{m,k}(n = 0)$, where a is the unit cell length along the nanoribbon, and n is the integer index of the unit cell.

4.3 Results and discussions

4.3.1 Magnetic field effect on interlayer transport

In this section, we will discuss the effect of magnetic field (B-field) on interlayer transmission, $T(E)$ of the mBGNRs. Since the interlayer transmission can be calculated from the wavefunctions and density-of-states of the individual nanoribbons, it is useful to understand the effect of a magnetic field on the individual nanoribbons. First, consider the energy-momentum $(E-k)$ dispersion relations resulting from the eigenvalues of H_k as a function of magnetic field. The band structures of the individual

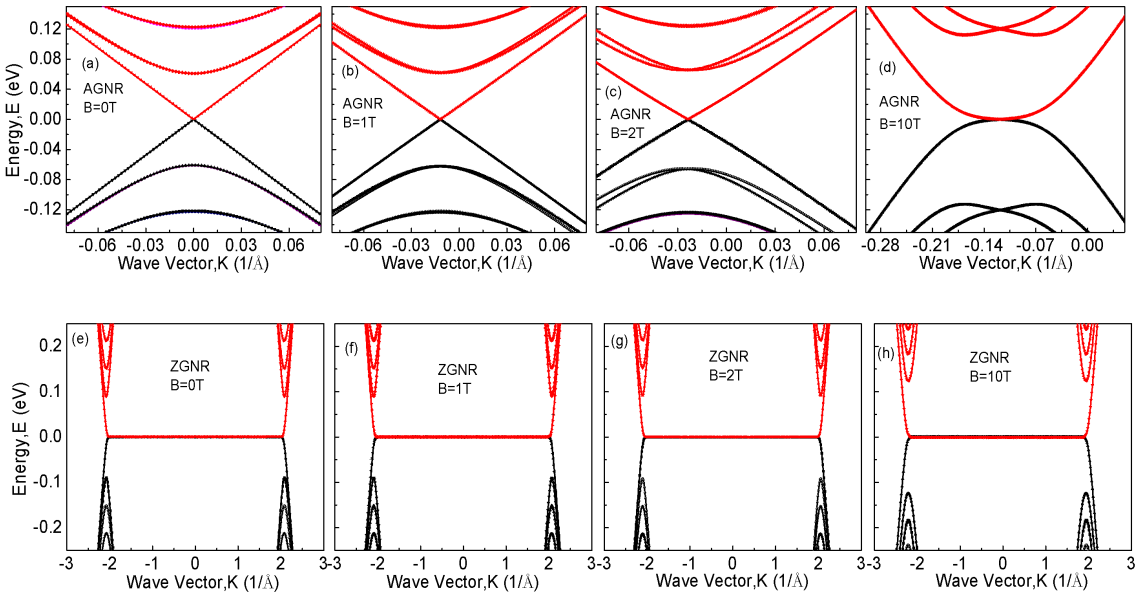

Figure 4.2: Energy band structure of 35nm individual single layer (a-d) AGNR and (e-f) ZGNR at B = 0T, 1T, 2T and 10T, respectively.

35nm wide AGNR and ZGNR are plotted at 4 values of perpendicular magnetic field as shown in Figs. 4.2 (a-d) and 4.2 (e-h), respectively. For AGNR, at low magnetic field (0-2T), the 2^{nd} subband appears at $\pm$ 0.06 eV as shown in Fig. 4.2(a-c). At higher magnetic fields (10T), the subbands shift to higher energies as Landau levels (LLs) begin to form. [82, 122, 123] Also, as the magnetic field increases (see Fig. 4.2(d)), the edge of the conduction band and the edge of the valence band flatten at the Dirac point.

For ZGNR, the electronic band structure exhibits a flat band at the charge neutral-

ity point even at B=0T due to the localized edge states [82,83]. At low magnetic field (0-2T), the 2^{nd} subband appears at ± 0.09 eV. Like the AGNR, at higher magnetic fields, the subbands of ZGNR move further away.

Tables

(i) Calculated $d_c(nm)$ and $E_L(eV)$					
B	0.5T	1T	2T	5T	10T
$d_c(nm)$	200	100	50	20	10
$E_L(eV)$	-	-	0.05, 0.13	0.08, 0.11	0.11, 0.16
(ii) Origin of steps (eV) observed in simulated $T(E)$					
$mBGNR$	$subband(AGNR)$	$subband(ZGNR)$	Landue Levels		
$35nm$	± 0.06	± 0.09		0.08, 0.11	0.11, 0.16
$50nm$	$\pm 0.04, \pm 0.08$	$\pm 0.65, \pm 0.1$	0.05, 0.13	0.08, 0.11	0.11, 0.16

Table 4.1: i) Calculated cyclotron diameters $d_c(nm)$ and the Landau level energies $E_L(eV)$ at different magnetic fields (ii) Origin of the steps (eV) observed in simulated transmission of the 35 nm and 50 nm mBGNR as shown in Figs. 4.5.

The LL formation can be further explained by the cyclotron diameter, d_c [124]. As d_c becomes smaller than the ribbon width (W), the cyclotron motion dominates and the LLs become well developed (see table 4.1 (i)). In the case of B<2T, the LLs are not perfectly formed and the band structure remains almost unchanged, because the edges interrupt the cyclotron motion of the electron. [82] For B>2T, where the ribbon width is sufficiently wide compared with the cyclotron diameter ($d_c \leq W$), the LLs are nearly developed result in flat band. From Figs. 4.2 (a-h), it is clearly understood that the applied B-field drastically modifies the energy bands by shifting

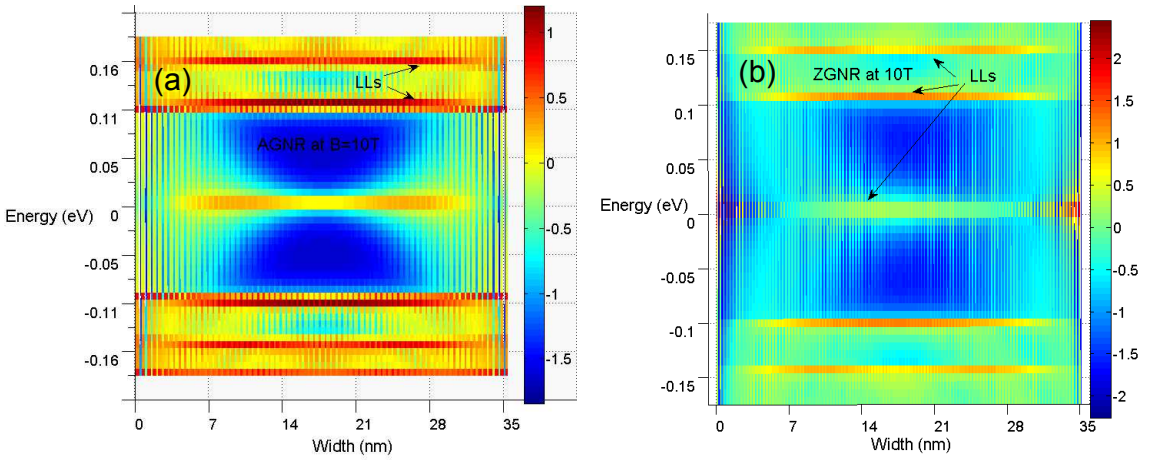

Figure 4.3: LDOS plot in color scale to demonstrate LLs bahaviour along the width direction for 35 nm (a) AGNR and (b) ZGNR at B = 10T.

the subbands, altering the band feature and creating discrete and well-separated LLs. This is also clearly understood from Table 4.1.

Now we will analyze the calculated spatial distribution of the local density of states (LDOS) of the mBGNRs. In Fig. 4.3 (a,b), we show the color scale plot of the LDOS along the width direction at B = 10 T for AGNR and ZGNR respectively. LLs are identified as the high intensity region of the color scale plot.

The density of states of the individual nanoribbons that appear in Eq. (4.4) are proportional to the inverse velocity $\sim (\partial E/\partial k)^{-1}$. When the slope is flat, the density of states is large, and Eq. (4.4) indicates that this could result in peaks in the transmission. This is what will be observed in the NEGF calculations of transmission. As the density of states of the armchair ribbon near the Dirac point increases with magnetic field, so also does the spatial overlap of the armchair and zigzag wavefunctions. Both wavefunctions become more localized near the edges of the nanoribbons. The spectral function $A_{i,i}(E)$ which is proportional to the squared magnitude of the wavefunction on each atom in the unit cell consisting of 4 atomic layers is plotted as a function of its x-coordinate across the width of the nanoribbon

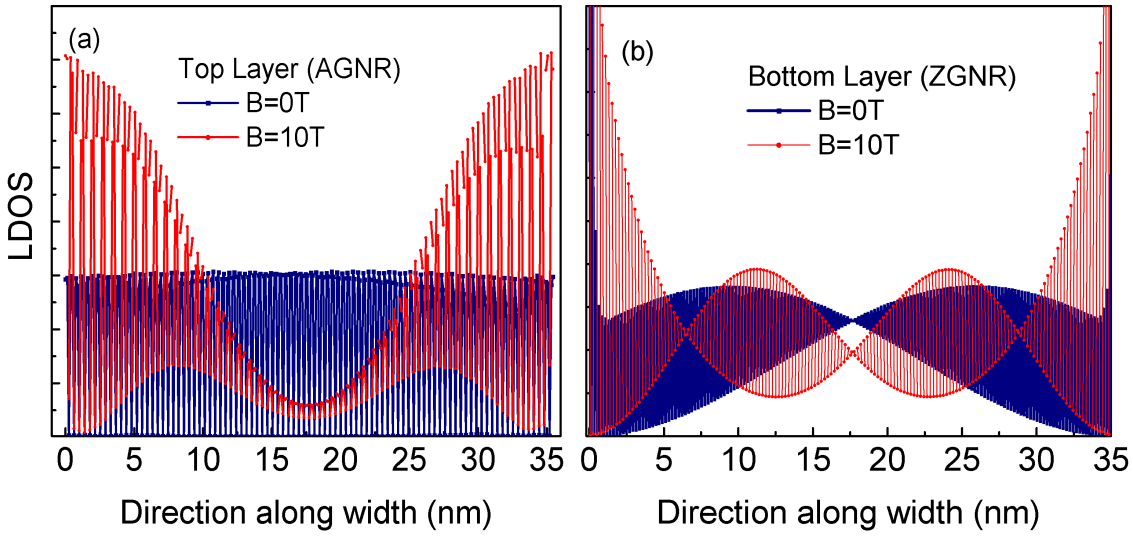

Figure 4.4: Spectral function of (a) the top AGNR and (b) the bottom ZGNR for the symmetric 35 nm mBGNR structure at two different magnetic fields of 0T and 10T at $E_f = 0.05$ eV.

in Fig. 4.4.

Figs. 4.4 (a) and (b) show the spatial distribution of the wavefunctions of the top (AGNR) and the bottom (ZGNR) layer of the 35 nm mBGNR respectively at magnetic fields of 0T and 10T near the charge neutrality point ($E = 0.05$ eV). At zero magnetic field, $|\psi|^2$ of the AGNR is distributed evenly across its width as shown in Fig. 4.4(a), whereas for the ZGNR, $|\psi|^2$ is more localized away from the center. This explains the observed flat bands in figure 4.2(e) are due to the edge states of the ZGNR. At a magnetic field of 10T, the magnitude of $|\psi|^2$ is maximum at the edges for both the AGNR and the ZGNR. The redistribution of the wavefunctions towards the edges of the GNRs and the flattening of the dispersion in Fig. 4.2(d) indicate that Landau levels and edge states are beginning to form. Therefore, electrons are transported mostly along the edges of the ribbon and that eliminates spatial overlap of the forward and backward transport states. As a result ballistic transport occurs

without scattering between the counter propagating edge states. For wider GNR structures (W = 50 nm, 70 nm) the Landau levels form at lower magnetic fields since the Landau levels begin to form when the cyclotron diameter becomes smaller than the ribbon width. [82, 124].

Now we will discuss the inter layer-transmission, $T(E)$, which describes the tunneling probability of an electron from the top layer (AGNR) to the bottom layer (ZGNR) of mBGNR (between contact 1 to 4 as shown in schematic 4.1). The expression for the transmission in Eq. (4.4) depends on both the joint density of states and the matrix element squared. As the magnetic field increases, the wavefunctions of both the AGNR and the ZGNR have a higher weight at the edges of the nanoribbon increasing their spatial overlap. Also, as discussed above, the joint density of states near the Dirac point increases. Thus, both the wavefunction and the density of state dependence on the magnetic field suggest that the interlayer transmission should increase near the Dirac point as the magnetic field increases.

The interlayer transmissions, $T(E)$ calculated from NEGF for the symmetric 35 nm, 50 nm, and 70 nm mBGNRs between contact 1 on the top AGNR and contact 4 on the bottom ZGNR (as shown in Fig. 4.1 (a)) are plotted in Fig.4.5 (a,b,c) for increasing values of magnetic field respectively. At $B = 0$T, the magnitude of $T(E)$ is low throughout the energy window except near the charge neutrality point (E = 0). Near the charge neutrality point, the transmission peaks result from the edge states localized at the ZGNR edges. The low magnitude of $T(E)$ is consistent with the electronic decoupling found in recent experimental [47] and theoretical studies [50] of twisted bilayer graphene.

The coherent, interlayer conductance at zero magnetic field and temperature of the 50 nm mBGNR at Fermi energies of 0.05 eV and 0.225 eV are ~ 1.9 S/cm^2 and ~ 100 S/cm^2, respectively. At higher Fermi energies, the coherent conductance increases

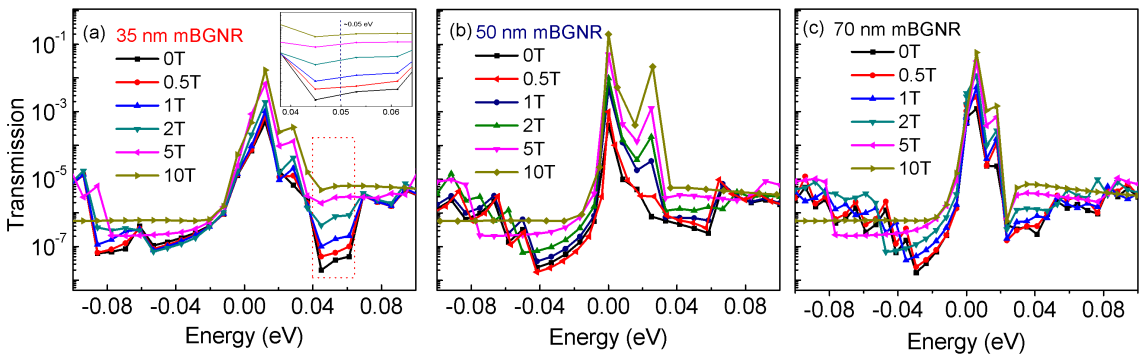

Figure 4.5: Transmission spectrum for different magnetic fields of the symmetric (a) 35nm (b) 50 nm and (c) 70 nm mBGNR structures.

due to the presence of excited subbands. Bistritzer and MacDonald [56] calculated an interlayer conductance between two infinite graphene sheets with a 30° misorientation angle and a Fermi energy of 0.26 eV of ~ 0.4 S/cm^2. Their result depends sensitively on their value of the finite lifetime broadening which was 75 meV, so that a direct comparison of quantitative values is, perhaps, not too meaningful. It is, however, possible that the finite size increases the interlayer conductance due to the presence of the zigzag edge states at low energy and multiple modes at higher energies. An increase in the coherent interlayer conductance per unit area with decreasing width is consistent with other calculations of crossed armchair nanoribbons a few nanometers wide. [11]

The room-temperature, interlayer conductance between infinite graphene sheets with a 30° misorientation angle is mediated by a 30 meV beating-mode, interface phonon resulting in a phonon-mediated conductance of $\sim 3 \times 10^5$ S/cm^2 at $E_F = 0.26$ eV. [125] This is 3 to 5 orders of magnitude larger than the coherent component of the conductance. Thus, low temperature and low bias are required to observe the coherent component of the conductance [125]. At low bias such that only the phonon adsorption channel is available, the phonon-mediated current is proportional

to the Bose-Einstein factor. Reducing the temperature from 300 K to 18 K reduces this factor by 10^8 which would allow the coherent component of the conductance to dominate throughout the energy spectrum.

The transmission for all structures in Fig. 4.5 is asymmetric around the charge neutrality point. Since the density of states of the individual GNRs are symmetric around the charge neutrality point, the matrix element in Eq. (4.4) must be asymmetric. The asymmetry indicates that the coupling of the conduction bands is stronger than that of valence bands. Further analysis of the asymmetry using Fermi's golden rule will be discussed later.

As the magnetic field is swept from 0 to 10 T, there can be several orders of magnitude change in the interlayer transmission (see inset of Fig. 4.5 (a)). The abrupt steps in transmission such as those of the 35 nm mBGNR at $\pm$ 0.06 eV and $\pm$ 0.09 eV result from the subbands in AGNR and ZGNR as previously discussed in Fig. 4.2. At the highest magnetic field of 10T, the increasing energy of the Landau levels pushes the first step to higher energies outside the domain of the graphs. The qualitative trends in the transmission spectrum remain the same for the wider 50 nm and 70 nm structures shown in Figs. 4.5 (b) and (c), respectively. The primary difference is that the transmission steps are more closely spaced since the subbands are closer in energy.

In the symmetric mBGNRs, the edge states of the ZGNR dominate the coherent transmission spectrum with peaks several orders of magnitude above the rest of the low-energy spectrum. To minimize the effect of the ZGNR edges, two different asymmetric mBGNR structures are considered where the ZGNR is wider than the AGNR. The two different structures consist of a 25 nm wide AGNR on a 50 nm wide ZGNR (50/25 mBGNR) and a 35 nm wide AGNR on a 70 nm wide ZGNR (70/35 mBGNR). Two qualitative trends in the transmission as a function of energy and magnetic field

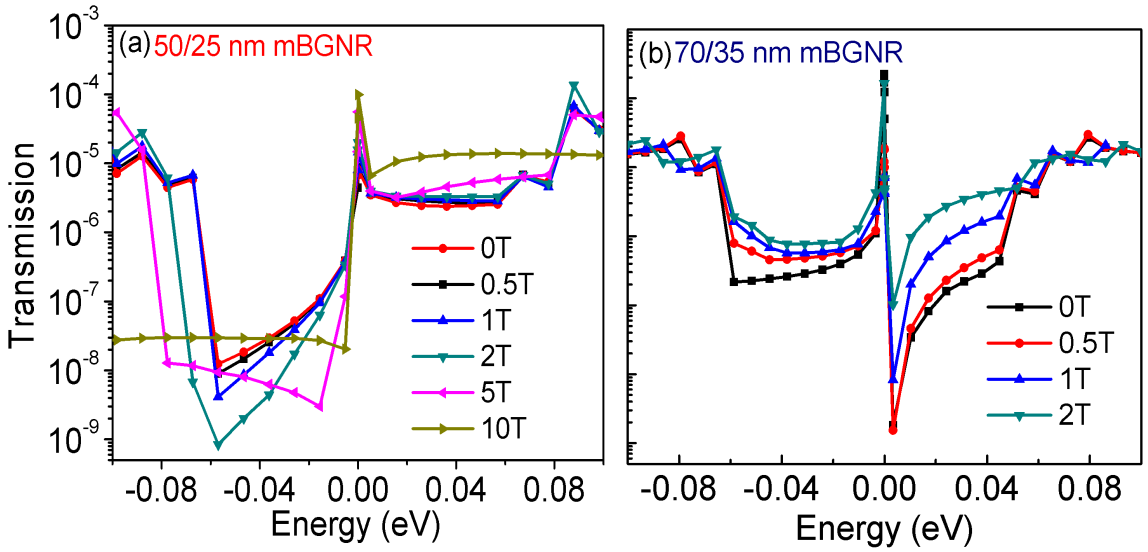

Figure 4.6: Transmission spectrum for different magnetic fields of the asymmetric (a) 50/25 nm mBGNR and (b) 70/35 nm mBGNR structures.

shown in Fig. 4.6 are similar to those of the symmetric mBNGRs. There is still large asymmetry between the electron and hole transmission. The change in the low-energy transmission with magnetic field is still large.

There are also qualitative differences. The peak in transmission becomes narrower as the zigzag edges are moved away from the overlap region. This is expected since the edge states decay exponentially into the body of the ribbon. In the largest structure, the asymmetry around the charge neutrality point switches such that the low-energy hole transmission is larger than the low-energy electron transmission. The line-shape of the transmission resembles that of a Fano resonance [126]. Such a resonance results from a localized state weakly coupled to the continuum. In this case, there is the localized zigzag edge state weakly coupled to the continuum state of the armchair nanoribbon.

To demonstrate that the Fermi's golden rule expression of Eq. (4.4) captures the essential physics of the interlayer transmission, the transmssions of the 50/25 nm

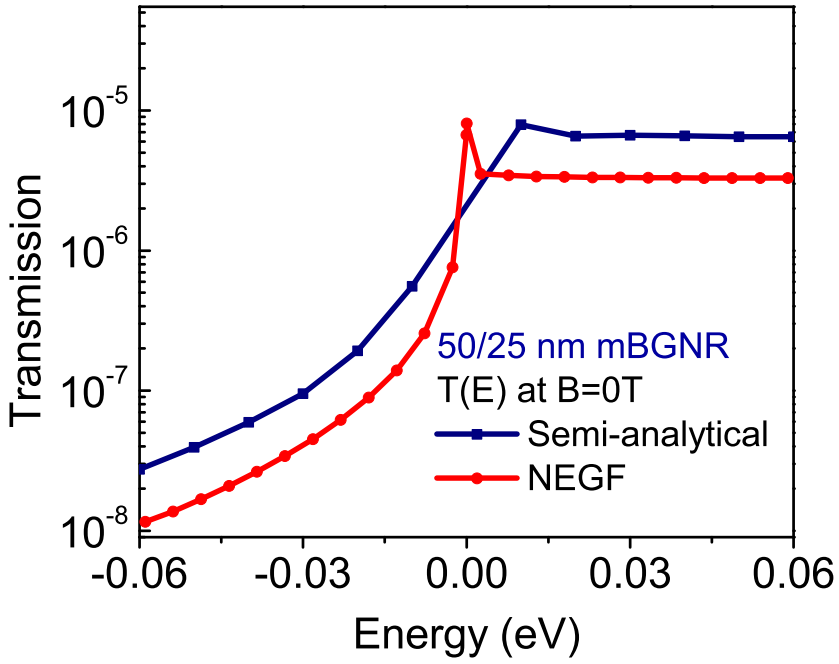

Figure 4.7: Comparison between analytical and simulated $T(E)$ of 50/25 nm mBGNR.

mBGNR structure calculated from Eqs. (4.4) and (4.1) are plotted in Fig. 4.7.

The semi-analytical transmission from Eq. (4.4) captures the qualitative trends of the transmission including the large asymmetry between the electron and hole transmission and the peak near the charge neutrality point. The asymmetry results from the matrix element. This is demonstrated by the plot of the matrix element squared shown in Fig. 4.8. This asymmetric nature results from the interlayer interaction and stacking geometry. Lu et al [100] studied the magneto-electronic properties of AA and ABC stacked graphite and found that the interlayer interactions destroy the symmetry about the Fermi level.

The coherent, interlayer magnetoconductance ratio as defined in Eq. (4.3) can be large. The zero-temperature, coherent magnetoconductance for 3 different structures with a Fermi energy of 0.05 eV is plotted versus magnetic field in Fig. 4.9 (a).

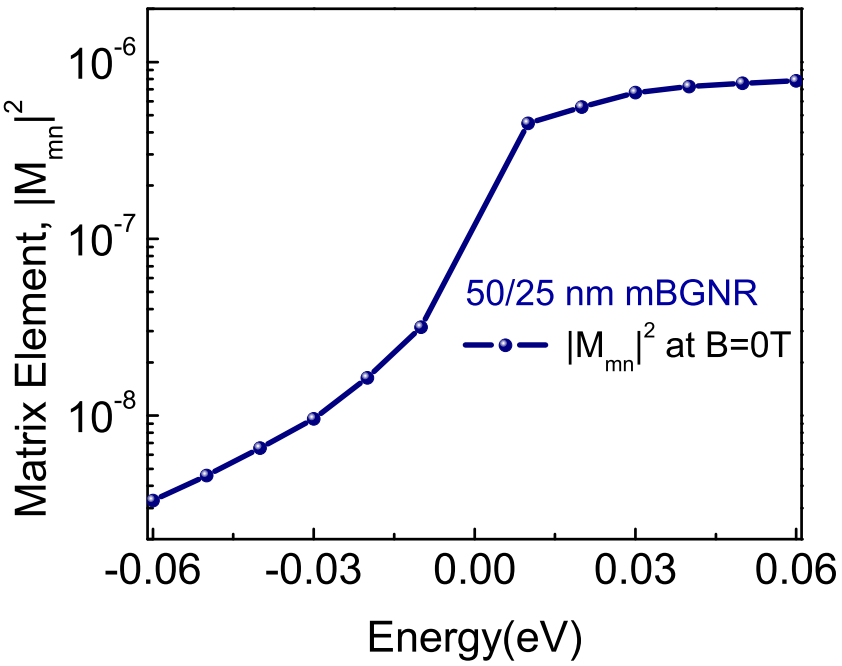

Figure 4.8: Matrix element square of 50/25 nm mBGNR.

The narrowest 35 nm structure has the largest magnetoconductance ratio, and the magnetoconductance ratio tends to decrease with increasing width. For the 35 nm mBGNR, the magnetoconductance ratio increased from 90% at 2T to 15,000% at 10T. The maximum magnetoconductance ratio at 10 T of the 50 nm structure is 1,300% and that of the 50/25 nm structure is 450%.

We also investigate the temperature dependence on MC ratio of the 50/25 nm mBGNR at $E_f = 0.035$ eV as shown in figure 4.9 (b). The MC ratio decreases as temperature increases from T = 4.2 K to 300 K. At room temperature, the MC ratio of the mBGNR is around 80% and 12% at 10T and 1T respectively. As the temperature increases, the Fermi level broadening causes the low-energy conductance to be dominated by the large peak at the charge-neutrality point. To the extent that this peak can be suppressed by moving the zizag edges farther away from the the

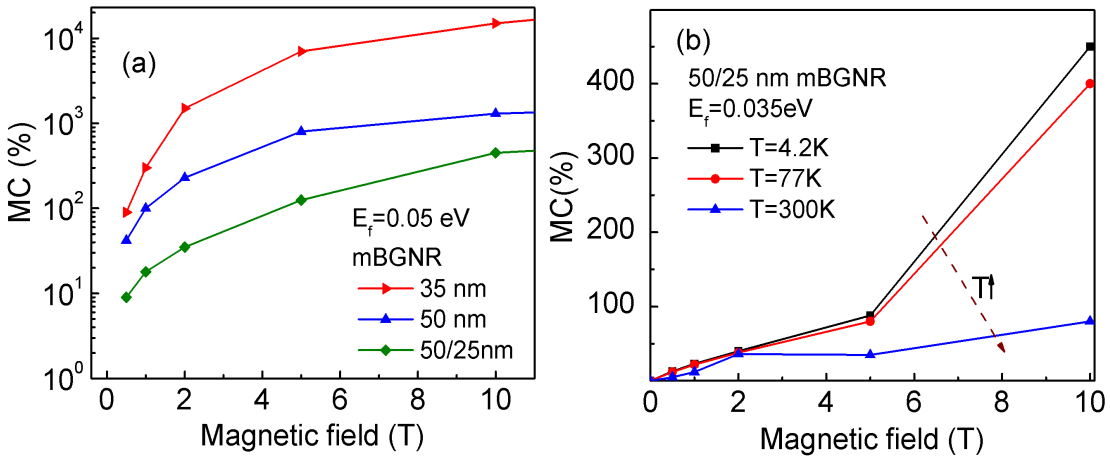

Figure 4.9: (a) Calculated MC ratio of different mBGNRs at $E_f = 0.05eV$ and (b) Temperature dependence of MC ratio of 50/25 nm mBGNR at $E_f = 0.035eV$.

overlap region, the larger the coherent magneto-conductance ratio can be.

4.3.2 Effect of interlayer potential difference

In this section, we will discuss the effect of the interlayer potential difference (V_b) on interlayer transmission, $T(E)$. To include V_b, we apply a finite voltage symmetrically between the top and the bottom layers of mBGNR. The site energies of the carbon atom of the top and bottom GNRs are rigidly shifted by $-eV_b/2$ and $eV_b/2$ respectively. Figure 4.10 shows the simulated transmission at different bias voltages of V_b = 0 V, 0.1 V and -0.1 V for an asymmetric 50/25 nm mBGNR.

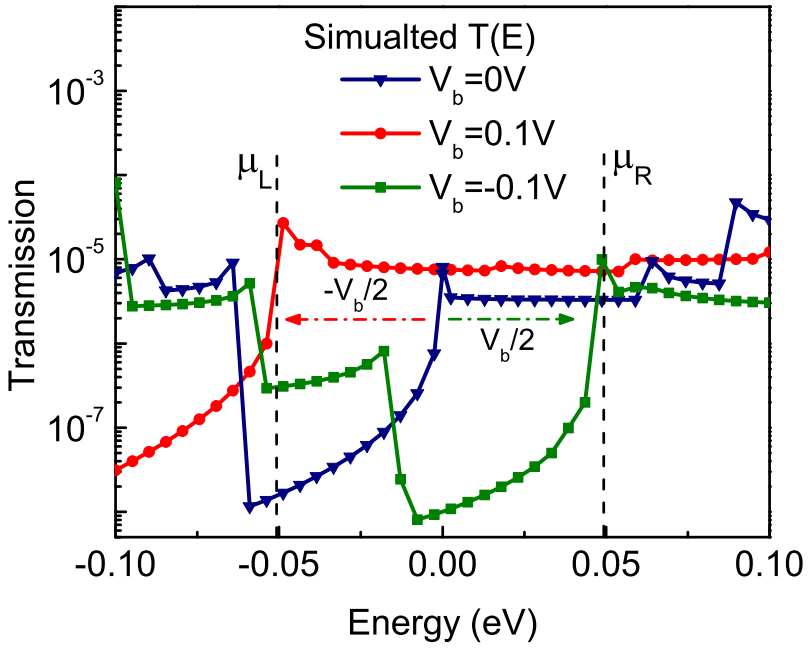

Figure 4.10: Effect of interlayer bias voltage (V_b) on simulated $T(E)$ of 50/25 nm mBGNR.

At $V_b = 0$V, the simulated transmission is asymmetric, and the peak is centered around the charge neutrality point (E = 0). With applied voltage (V_b), transmission peak is shifted by $-eV_b/2$. Under positive bias ($V_b = 0.1$V), the transmission peak is shifted to -0.05 V. The magnitude of the transmission increases by several order of magnitude within the energy transport window lying between the left and right Fermi levels, μ_L and μ_R, and the system becomes conductive. Under negative bias (V_b = -0.1V), the transmission peak is shifted to +0.05 V, and due to the asymmetry, the transmission is strongly suppressed withing the energy transport window. Therefore, a positive bias enhances the transmission whereas a negative bias suppresses the transmission within the energy window.

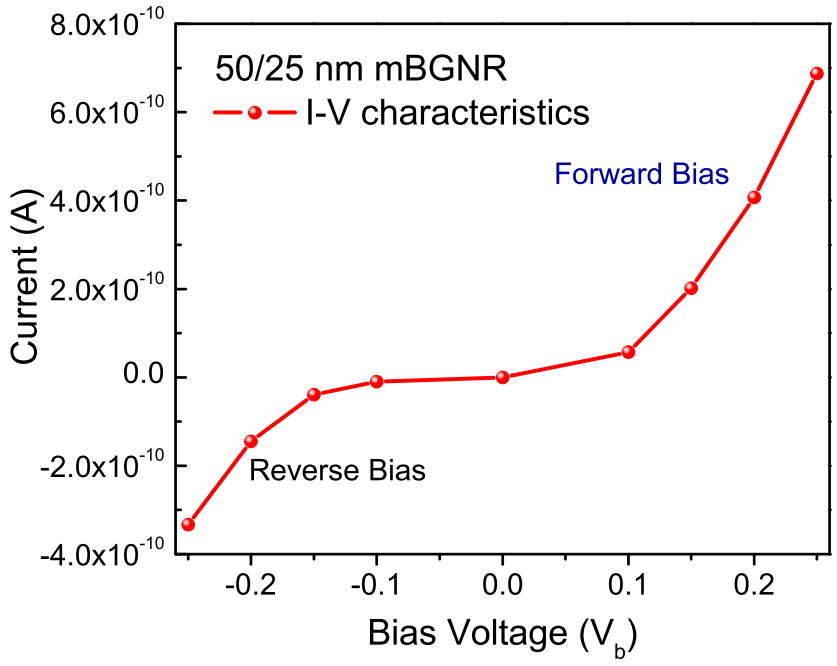

Figure 4.11: Calculated $I-V$ characteristics 50/25 nm mBGNR showing non-linear diode characteristics

The $I-V$ characteristic resulting from varying the bias voltage V_b from -0.25 V to 0.25 V is shown in Fig. 4.11. The calculated I-V characteristic shows some non-linear diode-like behavior at low bias and room temperature. This behavior is more pronounced at low temperature when the 50 meV energy window shown in Fig. 4.10 is much greater than k_BT.

4.4 Conclusions

We investigated the interlayer transport properties of both symmetric and asymmetric mBGNR structures under applied perpendicular magnetic field and interlayer bias. The coherent, interlayer conductance of misoriented graphene nanoribbons is a strong

function of energy and magnetic field. Experimental observation will require low temperature (< 20 K) and low bias (< 30 mV) to remove the phonon-mediated channel. When edge states are present in or near the overlap region, they result in a large peak in the coherent interlayer transmission at the charge neutrality point. The peak is several orders of magnitude larger than the surrounding low-energy transmission spectrum. The width of the peak is reduced as the edge states are moved away from the overlap region, since the edge states decay exponentially into the nanoribbon. The coherent interlayer conductance is consistently asymmetric around the charge neutrality point for all structures with the value differing by up to 3 orders of magnitude at $E_F = \pm 0.05$ eV. Since the density of states of the individual GNRs is symmetric, the asymmetry results from the matrix element of the wavefunctions. In the 70/35 nm mBGNR structure in which the zigzag edge states have been moved the furthest from the overlap region, the asymmetry appears as a Fano resonance. This is consistent with the localized edge states being weakly coupled to the continuum states in the overlap region. The low-energy states exhibit a high magnetoconductance ratio at low temperature, and the magnetoconductance ratio tends to increase as the width of the nanoribbons decrease. The maximum value at 10 T is 15,000%. The transmission can be modulated by the interlayer bias. The calculated $I - V$ characteristics of the mBGNR are asymmetric with rectifying behavior.

Chapter 5

Conclusion

In summary, we study the electronic and magnetic properties of nano patterned graphene based structures using extended Huckel and empirical tight-binding models. Three different structures were investigated for creating a bandgap. Significant bandgap opening is observed in all proposed structures. Dangling bonds at the unpassivated edges of an AGNR create extra modes in the channel region, and that they are removed by H passivation. The magnitude of effective mass is inversely proportional to the width of the AGNR. External bias has a significant effect on the bandstructure of bilayer GNRs. Based on this property we considered a device of two stacked monolayers of AGNR termed a s-AGNR device. The stacked device shows negative differential resistance (NDR) behavior. The magnitude of the NDR decreases with increased ribbon width. Finally, we study method of tuning the bandgap in a 2D graphene nanomesh. consisting of uniformly distributed holes in a graphene sheet. The bandgap is governed by the spacing between the holes, and a spacing of 22 Å results in a bandgap of about 0.1 eV.

In the second part of the dissertation, we describe an unconventional approach of modulating current voltage characteristics without inducing a bandgap. Both single-

layer and bilayer graphene FETs are considered, and NDR is observed on both devices in a diode-connected biasing scheme in the quantum capacitance limit. The largest peak-to-valley current ratio occurs in the BLGFET when the two layers are at the same potential. To create a bandgap in the BLG using the gate voltage, one must sacrifice some fraction of the potential control of the channel. To create a maximum potential difference between the two graphene sheets of a BLGFET, one must sacrifice half of the potential control of the channel. The benefit of inducing a bandgap with gate voltage is outweighed by the cost of losing potential control of the channel. The net result is a reduction in the magnitude of the NDR. The peak-to-valley difference increases for increasing doping concentration of graphene sheets.

Finally we investigated the interlayer transport properties of both symmetric and asymmetric misoriented bilayer graphene nanoribbons under applied perpendicular magnetic field and interlayer bias. The coherent, interlayer conductance of misoriented graphene nanoribbons is a strong function of energy and magnetic field. Experimental observation will require low temperature (< 20 K) and low bias (< 30 mV) to remove the phonon-mediated channel. When edge states are present in or near the overlap region, they result in a large peak in the coherent interlayer transmission at the charge neutrality point. The peak is several orders of magnitude larger than the surrounding low-energy transmission spectrum. The width of the peak is reduced as the edge states are moved away from the overlap region, since the edge states decay exponentially into the nanoribbon. The coherent interlayer conductance is consistently asymmetric around the charge neutrality point for all structures with the value differing by up to 3 orders of magnitude at $E_F = \pm 0.05$ eV. Since the density of states of the individual GNRs is symmetric, the asymmetry results from the matrix element of the wavefunctions. In the structure in which the zigzag edge states have been moved the furthest from the overlap region, the asymmetry appears as a Fano

resonance. This is consistent with the localized edge states being weakly coupled to the continuum states in the overlap region. The low-energy states exhibit a high magnetoconductance ratio at low temperature, and the magnetoconductance ratio tends to increase as the width of the nanoribbons decrease. The maximum value at 10T is 15,000%. The transmission can be modulated by the interlayer bias. The calculated I-V characteristics of the mBGNR are asymmetric with rectifying behavior.

Bibliography

[1] G. Liu, S. Ahsan, A. G. Khitun, R. K. Lake, and A. A. Balandin, "Graphene-based non-boolean logic circuits," *J. Appl. Phys.*, vol. 114, p. 154310, 2013.

[2] S. Ahsan, K. M. M. Habib, M. R. Neupane, and R. K. Lake, "Interlayer magnetoconductance of misoriented bilayer graphene ribbons," *J. Appl. Phys.*, vol. 114, pp. 183 711–7, 2013.

[3] Y. W. Son, M. Cohen, and S. G. Louie, "Energy gaps in graphene nanoribbons," *Phys. Rev. Lett. 97*, vol. 97, p. 216803, 2006.

[4] International Technology Roadmap for Semiconductors 2009 Ed. Emerging Research Devices. www.itrs.net/Links/2009ITRS.

[5] V. V. Zhirnov and R. K. Cavin, "J. nanoelectron optoelectron," *1*, vol. 52, 2006.

[6] S. Iijima, "Helical microtubules of graphitic carbon," *Nature*, vol. 354, pp. 56–58, 1991.

[7] J. Appenzeller, Y.-M. Lin, J. Knoch, Z. Chen, and P. Avouris, "Comparing carbon nanotube transistors - the ideal choice: a novel tunneling device design," *IEEE Trans. Elect. Dev.*, vol. 52, no. 12, pp. 2568 – 2576, 2005.

[8] K. S. Novoselov, A. K. Geim, S. V. Morozov, D. Jiang, Y. Zhang, S. V. Dubonos, I. V. Grigorieva, and A. A. Firsov, "Electric Field Effect in Atomically Thin Carbon Films," *Science*, vol. 306, no. 5696, pp. 666–669, 2004.

[9] A. K. Geim, *Science*, vol. 324, p. 1530, 2009.

[10] B. Huard, J. A. Sulpizio, N. Stander, K. Todd, B. Yang, and D. Goldhaber-Gordon, *Phys. Rev. Lett.*, vol. 98, p. 236803, 2007.

[11] K. M. M. Habib and R. K. Lake, "Current modulation by voltage control of the quantum phase in crossed graphene nanoribbons," *Phys. Rev. B*, vol. 86, p. 045418, 2012.

[12] W. Long, Q. F. Sun, and J. Wang, *Phys. Rev. Lett.*, vol. 101, p. 205308, 2008.

[13] Q. Zhang, D. Fu, B. Wang, R. Zhang, and D. Y. Xing, *Phys. Rev. Lett.*, vol. 101, p. 047005, 2008.

[14] Z. H. N. et al., *Nano Letters*, vol. 10, p. 38683872, 2010.

[15] K. S. Novoselov, A. K. Geim, S. V. Morozov, D. Jiang, M. I. Katsnelson, I. V. Grigorieva, S. V. Dubonos, and A. A. Firsov, "Two-dimensional gas of massless dirac fermions in graphene," *Nature*, vol. 438, p. 197, 2005.

[16] Y. Zhang, Y. W. Tan, H. L. Stormer, and P. Kim, "Experimental observation of the quantum hall effect and berry's phase in graphene," *Nature*, vol. 438, p. 201, 2005.

[17] V. P. Gusynin and S. G. Sharapov, "Unconventional integer quantum hall effect in graphene," *Phys. Rev. Lett.*, vol. 95, p. 146801, 2005.

[18] A. F. Morpurgo, "Dirac electrons broken to pieces," *Nature (London)*, vol. 462, p. 170, 2009.

[19] C. Toke, P. E. Lammert, V. H. Crespi, and J. K. Jain, "Fractional quantum hall effect in graphene," *Phys. Rev. B*, vol. 74, p. 235417, 2006.

[20] A. K. Geim and K. S. Novoselov, *Nature Mater.*, vol. 6, p. 183, 2007.

[21] R. R. e. a. Nair, *Science*. 320, 2008.

[22] A. A. Balandin, *Nat. Mater.*, vol. 10, pp. 569–581, 2011.

[23] F. Xia, D. B. Farmer, Y. Lin, and P. Avouris, *Nano Letter*, vol. 10, pp. 715–718, 2010.

[24] M. Han, B. Ozyilmaz, Y. Zhang, and P. Kim, *Physical Review Letter*, vol. 98, p. 206805, 2007.

[25] B. N. Szafranek, D. Schall, M. Otto, D. Neumaier, and H. Kurz, *Nano Letter*, vol. 11, p. 2640, 2011.

[26] S.M.Choi, S. Jhi, and Y. Son, *Nano Letter*, vol. 10, p. 3486, 2010.

[27] K.-T. Lam and G. Liang, "An ab initio study on energy gap of bilayer graphene nanoribbons with armchair edges," *Applied Physics Letters*, vol. 92, no. 22, p. 223106, 2008.

[28] C. L. Lu, C. P. Chang, Y. C. Huang, J. M. Lu, C. C. Hwang, and M. F. Lin, "Low-energy electronic properties of the ab-stacked few-layer graphites," *Journal of Physics: Condensed Matter*, vol. 18, no. 26, p. 5849, 2006. [Online]. Available: http://stacks.iop.org/0953-8984/18/i=26/a=005

[29] H. Min, B. Sahu, S. K. Banerjee, and A. H. MacDonald, "Ab initio theory of gate induced gaps in graphene bilayers," *Phys. Rev. B*, vol. 75, no. 15, p. 155115, Apr 2007.

[30] Y. Zhang, T.-T. Tang, C. Girit, Z. Hao, M. C. Martin, A. Zettl, M. F. Crommie, Y. R. Shen, and F. Wang, "Direct observation of a widely tunable bandgap in bilayer graphene," *Nature*, vol. 459, no. 7248, p. 820, 2009.

[31] G. Fiori and G. Iannaccone, "On the possibility of tunable-gap bilayer graphene fet," *IEEE Elect. Dev. Lett.*, vol. 30, no. 3, pp. 261–264, March 2009.

[32] ——, "Ultralow-voltage bilayer graphene tunnel fet," *IEEE Elect. Dev. Lett.*, vol. 30, no. 10, pp. 1096–1098, Oct 2009.

[33] K.-T. Lam and G. Liang, "A computational evaluation of the designs of a novel nanoelectromechanical switch based on bilayer graphene nanoribbon," in *IEEE Int. Electron Devices Meeting Tech. Dig.* New York: IEEE, 2009, pp. 37.3.1 – 37.3.4.

[34] J. R. Williams, L. DiCarlo, and C. M. Marcus, "Quantum hall effect in a gate-controlled p-n junction of graphene," *Science*, vol. 317, no. 5838, pp. 638–641, 2007. [Online]. Available: http://www.sciencemag.org/content/317/5838/638.abstract

[35] R. V. Gorbachev, A. S. Mayorov, A. K. Savchenko, D. W. Horsell, and F. Guinea, "Conductance of p-n-p graphene structures with "air-bridge" top gates," *Nano Letters*, vol. 8, no. 7, pp. 1995–1999, 2008, pMID: 18543979. [Online]. Available: http://pubs.acs.org/doi/abs/10.1021/nl801059v

[36] S. Banerjee, L. F. Register, E. Tutuc, D. Reddy, and A. H. MacDonald, "Bilayer pseudospin field-effect tran- sistor (bisfet): A proposed new logic device," *IEEE Elect. Dev. Lett.*, vol. 30, no. 2, 2009.

[37] V. N. Do and P. Dollfus, "Negative differential resistance in zigzag-edge graphene nanoribbon junctions," *Journal of Applied Physics*, vol. 107, no. 6, p. 063705, 2010.

[38] H. Ren, Q.-X. Li, Y. Luo, and J. Yang, "Graphene nanoribbon as a negative differential resistance device," *Applied Physics Letters*, vol. 94, no. 17, p. 173110, 2009.

[39] H. Fang, R. Z. Wang, S. Y. Chen, M. Yan, X. M. Song, and B. Wang, *Strain-induced negative differential resistance in armchair-edge graphene nanoribbons*, 2011, vol. 98, no. 8.

[40] V. H. Nguyen, A. Bournel, and P. Dollfus, "Large peak-to-valley ratio of negative-differential-conductance in graphene p-n junctions," *Applied Physics Letters*, vol. 109, no. 9, p. 093706, 2011. [Online]. Available: http://dx.doi.org/doi/10.1063/1.3587570

[41] L. Britnell, R. V. Gorbachev, R. Jalil, B. D. Belle, F. Schedin, A. Mishchenko, T. Georgiou, M. I. Katsnelson, L. Eaves, S. V. Morozov, N. M. R. Peres, J. Leist, A. K. Geim, K. S. Novoselov, and L. A. Ponomarenko, "Field-effect tunneling transistor based on vertical graphene heterostructures," *Science*, vol. 335, no. 6071, pp. 947–950, 2012.

[42] T. Sohier and B. Yu, "Ultralow-voltage design of graphene pn junction quantum reflective switch transistor," *Applied Physics Letters*, vol. 98, no. 21, p. 213104, 2011.

[43] M. Gilbert, "Performance characteristics of scaled bilayer graphene pseudospin devices," *Electron Devices, IEEE Transactions on*, vol. 57, no. 11, pp. 3059 –3067, nov. 2010.

[44] C. Berger, Z. Song, X. Li, X. Wu, N. Brown, C. Naud, D. Mayou, T. Li, J. Hass, A. N. Marchenkov, E. H. Conrad, P. N. First, and W. A. de Heer, "Electronic confinement and coherence in patterned epitaxial graphene," *Science*, vol. 312, 2006.

[45] J. Hass, R. Feng, J. E. Millan-Otoya, X. Li, M. Sprinkle, P. N. First, W. A. de Heer, E. H. Conrad, and C. Berger, "Structural properties of the multilayer graphene/ 4h-sic(0001) system as determined by surface x-ray diffraction," *Phys. Rev. B*, vol. 75, p. 214109, 2007.

[46] J. Hass, F. Varchon, J. E. M. Otoya, M. Sprinkle, N. Sharma, W. A. de Heer, C. Berger, P. N. First, L. Magaud, and E. H. Conrad, "Why multilayer graphene on 4h-sic(0001) behaves like a single sheet of graphene," *Phys. Rev. Lett.*, vol. 100, p. 125504, 2008.

[47] A. Luican, G. Li, A. Reina, J. Kong, R. R. Nair, K. S. Novoselov, A. K. Geim, and E. Y. Andrei, "Single-layer behavior and its breakdown in twisted graphene layers," *Phys. Rev. Lett.*, vol. 106, p. 126802, 2011.

[48] X. Wu, X. Li, Z. Song, C. Berger, and W. A. de Heer, "Weak antilocalization in epitaxial graphene: Evidence for chiral electrons," *Phys. Rev. Lett.*, vol. 98, p. 136801, 2007.

[49] S. Latil, V. Meunier, and L. Henrard, "Massless fermions in multilayer graphitic systems with misoriented layers: Ab initio calculations and experimental fingerprints," *Phys. Rev. B*, vol. 76, p. 201402, 2007.

[50] S. Shallcross, S. Sharma, and O. A. Pankratov, "Quantum interference at the twist boundary in graphene," *Phys. Rev. Lett.*, vol. 101, p. 056803, 2008.

[51] Z. Ni, Y. Wang, T. Yu, Y. You, and Z. Shen, "Reduction of fermi velocity in folded graphene observed by resonance raman spectroscopy," *Phys. Rev. B*, vol. 77, p. 235403, 2008.

[52] R. Zhao, Y. Zhang, T. Gao, Y. Gao, N. Liu, L. Fu, and Z. Liu, "Scanning tunneling microscope observations of non-ab stacking of graphene on ni films," *Nano Res.*, vol. 4, p. 712, 2011.

[53] L. Xie, H. Wang, C. Jin, X. Wang, L. Jiao, K. Suenaga, and H. Dai, "Graphene nanoribbons from unzipped carbon nanotubes: Atomic structures, raman spectroscopy, and electrical properties," *J. Am. Chem. Soc.*, vol. 133, p. 10394, 2011.

[54] S. Shallcross, S. Sharma, E. Kandelaki, and O. A. Pankratov, *Phys. Rev. B*, vol. 81, p. 165105, 2010.

[55] J. M. B. L. dos Santos, N. M. R. Peres, and A. H. C. Neto, *Phys. Rev. Lett*, vol. 99, p. 256802, 2007.

[56] R. Bistritzer and A. H. MacDonald, "Transport between twisted graphene layers," *Phys. Rev. B*, vol. 81, p. 245412, 2010.

[57] V. Perebeinos, J. Tersoff, and P. Avouris, "Phonon-mediated interlayer conductance in twisted graphene bilayers," *Phys. Rev. Lett.*, vol. 109, p. 236604, 2012.

[58] W. Y. Kim and K. S. Kim, "Prediction of very large values of magnetoresistance in a graphene nanoribbon device," *Nature Nanotechnology*, vol. 3, p. 408, 2008.

[59] F. M. Rojas, J. F. Rossier, and J. J. Palacios, "Giant magnetoresistance in ultrasmall graphene based devices," *Phys. Rev. Lett.*, vol. 102, p. 136810, 2009.

[60] G. Li and E. Y. Andrei, "Observation of landau levels of dirac fermions in graphite," *Nature Phys.*, vol. 3, p. 623, 2007.

[61] W. H. Wang, K. Pi, Y. Li, Y. F. Chiang, P. Wei, J. Shi, and R. K. Kawakami, "Magnetotransport properties of mesoscopic graphite spin valves," *Phys. Rev. B*, vol. 77, p. 020402(R), 2008.

[62] E. W. Hill, A. K. Geim, K. Novoselov, F. Schedin, and P. Black, "Graphene spin valve devices," *IEEE Trans. Magn.*, vol. 42, p. 2694, 2006.

[63] J. Bai, R. Cheng, F. Xiu, L. Liao, M. Wang, A. Shailos, K. L. Wang, Y. Huang, and X. Duan, "Very large magnetoresistance in graphene nanoribbons," *Nature Nanotechnology*, vol. 5(9), pp. 655, 1, 79, 2010.

[64] K. H. Ding, Z. G. Zhu, and J. Berakdar, "Magnetotransport through graphene spin valves," *Phys. Rev. B*, vol. 79, p. 045405, 2009.

[65] L. Brey and H. A. Fertig, "Magnetoresistance of graphene-based spin valves," *Phys Rev. B*, vol. 76, p. 205435, 2007.

[66] A. Saffarzadeh and M. G. Asl, "Spin currents and magnetoresistance of graphene-based magnetic junctions," *Eur Phys. J. B*, vol. 67, no. 239, 2009.

[67] H. Santos, L. Chico, and L. Brey, "Carbon nanoelectronics: Unzipping tubes into graphene ribbons," *Phys. Rev. Lett.*, vol. 103, p. 086801, 2009.

[68] E. H. Hwang and S. D. Sarma, "Graphene magnetoresistance in a parallel magnetic field: Spin polarization effect," *Phys. Rev. B*, vol. 80, p. 075417, 2009.

[69] J. Bai, X. Zhong, S. Jiang, Y. Huang1, and X. Duan, "Graphene nanomesh," *Nature nanotechnology*, vol. 5, p. 190, 2010.

[70] J. C. Slater, "Atomic shielding constants," *Phys. Rev.*, vol. 36, p. 57, 1930.

[71] R. S. Mullekin, C. A. Rieke, and H. Orloff, "Formulas and Numerical Tables for Overlap Integrals," *The Journal of Chemical Physics*, vol. 17, no. 12, December 1949.

[72] M. Galperin, S. Toledo, and A. Nitzan, "Numerical computation of tunneling fluxes," *J. Chem. Phys.*, vol. 117, pp. 10 817–10 826, 2002.

[73] M. P. L. Sancho, J. M. L. Sancho, and J. Rubio, "Highly convergent schemes for the calculation of bulk and surface green functions," *J. Phys. F*, vol. 15, pp. 851–858, 1985.

[74] N. Bruque, R. R. Pandey, R. Lake, H. Wang, and J. Lewis, "Electronic transport through a cnt-pseudopeptide-cnt hybrid material," *Molecular Simulation*, vol. 31, no. 12, pp. 859 – 864, 2005. [Online]. Available: dx.doi.org/10.1080/08927020500323879

[75] R. R. Pandey, N. Bruque, K. Alam, and R. Lake, "Carbon nanotube - molecular resonant tunneling diode," *Phys. Stat. Sol. (a)*, vol. 203, no. 2, pp. R5 – R7, 2006. [Online]. Available: http://dx.doi.org/10.1002/pssa.200521467

[76] N. A. Bruque, K. Alam, R. R. Pandey, R. K. Lake, J. P. Lewis, X. Wang, F. Liu, C. S. Ozkan, M. Ozkan, and K. L. Wang, "Self-assembled carbon nanotubes for electronic circuit and device applications," *J. Nanoelectronics Optoelectronics*, vol. 1, no. 1, pp. 74 – 81, 2006. [Online]. Available: http://dx.doi.org/10.1166/jno.2006.007

[77] R. Lake, G. Klimeck, R. C. Bowen, and D. Jovanovic, "Single and multiband modeling of quantum electron transport through layered semiconductor devices," *J. Appl. Phys.*, vol. 81, no. 12, pp. 7845–7869, 1997.

[78] D. S. Fisher and P. A. Lee, "Relation between conductivity and transmission matrix," *Phys. Rev. B*, vol. 23, no. 12, pp. 6851–4, 1981.

[79] C. Caroli, R. Combescot, P. Nozieres, and D. Saint-James, "Direct calculation of the tunneling current," *J. Phys. C: Solid State Physics*, vol. 4, pp. 916–929, 1971.

[80] D. Lohez and M. Lannoo, "Generalization of the Green's-functions formalism to nonorthogonal orbitals: Application to amorphous SiO_2," *Phys. Rev. B*, vol. 27, no. 8, pp. 5007–5011, 1983.

[81] K. Nakada and M. Fujita, "Edge state in graphene ribbons: Nanometter size effect and edge shape dependence," *Phys. Rev. B*, vol. 54, no. 24, pp. 17 954–17 961, 1996.

[82] K. Wakabayashi, M. Fujita, H. Ajiki, and M. Sigrist, "Electronic and magnetic properties of nanographite ribbons," *Phys. Rev. B*, vol. 59, p. 8271, 1999.

[83] M. Fujita, K. Wakabayashi, K. Nakada, and K. Kusakabe, "Peculiar localized state at zigzag graphite edge," *J. Phys Soc. Jpn.*, vol. 65, p. 1920, 1996.

[84] M. Ezawa, *Phys. Rev. B*, vol. 73, p. 045432, 2006.

[85] H. Ajiki and T. Ando, "Energy gaps in graphene nanoribbons," *J. Phys. Soc. Jpn.*, vol. 62, p. 1255, 1992.

[86] K. M. M. Habib, F. Zahid, and R. K. Lake, "Negative differential resistance in bilayer graphene nanoribbons," *Applied Physics Letters*, vol. 98, no. 19, p. 192112, 2011.

[87] G. Fiori, "Negative differential resistance in mono and bilayer grapahene p-n junctions," *IEEE Electron Device Letters*, vol. 32, no. 10, October 2011.

[88] L. Liao, Y.-C. Lin, M. Bao, R. Cheng, J. Bai, Y. Liu, Y. Qu, K. L. Wang, Y. Huang, and X. Duan, "High-speed graphene transistors with a self-aligned nanowire gate," *Nature*, vol. 467, no. 16, p. 305308, 2010.

[89] K. Jenkins, D. Farmer, A. Valdes-Garcia, P. Avouris, C.-Y. Sung, H.-Y. Chiu, and B. Ek, "Development of graphene fets for high frequency electronics," *IEDM*, pp. 237–240, Dec. 2009.

[90] I. Meric, N. Baklitskaya, P. Kim, and K. L. Shepard, "Rf performance of top-gated, zero-bandgap graphene field-effect transistors," *IEDM*, p. 4796738, 2008.

[91] A. Rahman, J. Guo, S. Datta, and M. S. Lundstrom, "Theory of ballistic nanotransistors," *IEEE Trans. Elect. Dev.*, vol. 50, no. 9, pp. 1853 – 1864, 2003.

[92] J. M. B. Lopes dos Santos, N. M. R. Peres, and A. H. Castro Neto, "Continuum model of the twisted graphene bilayer," *Phys. Rev. B*, vol. 86, p. 155449, Oct 2012. [Online]. Available: http://link.aps.org/doi/10.1103/PhysRevB.86.155449

[93] S. Shallcross, S. Sharma, E. Kandelaki, and A. Pankratov O., "Electronic structure of turbostratic graphene," *Phys. Rev. B*, vol. 81, p. 165105, Apr 2010. [Online]. Available: http://adsabs.harvard.edu/abs/2010PhRvB..81p5105S

[94] S. Shallcross, S. Sharma, and O. Pankratov, "Emergent momentum scale, localization, and van hove singularities in the graphene twist bilayer," *Phys. Rev. B*, vol. 87, p. 245403, Jun 2013.

[95] D. Chae, D. Zhang, X. Huang, and K. V. Klitzing, "Electronic transport in two stacked graphene monolayers," *Nano Lett.*, vol. 12, p. 3905, 2012.

[96] Y. R. Hernandez, S. Schweitzer, J.-S. Kim, A. K. Patra, J. Englert, I. Lieberwirth, A. Liscio, V. Palermo, X. Feng, A. Hirsch, M. Kläui, and K. Müllen, "Turbostratic graphitic microstructures: electronically decoupled multilayer graphene devices with robust high charge carrier mobility," *arXiv:1301.6087*, pp. 1 – 14, 2013.

[97] Y. Kim, H. Yun, S.-G. Nam, M. Son, D. S. Lee, D. C. Kim, S. Seo, H. C. Choi, H.-J. Lee, S. W. Lee, and J. S. Kim, "Breakdown of the interlayer coherence in twisted bilayer graphene," *Phys. Rev. Lett.*, vol. 110, p. 096602, Feb 2013. [Online]. Available: http://link.aps.org/doi/10.1103/PhysRevLett.110.096602

[98] E. McCann and V. Falko, "Landau-level degeneracy and quantum hall effect in a graphite bilayer," *Phys. Rev. Lett.*, vol. 96, p. 086805, 2006.

[99] C. Chang, C. Lu, F. Shyu, R. Chen, Y. Huang, and M. Lin, "Magnetoelectronic properties of nanographite ribbons," *Physica E*, vol. 27, p. 82, 2005.

[100] C. L. Lu, C. P. Chang, and M. F. Lin, "Magneto-electronic properties of the aa- and abc-stacked graphites," *The European Phys. Journal B*, vol. 60, p. 161, 2007.

[101] Y. W. Son, M. L. Cohen, and S. G. Louie, "Half-metallic graphene nanoribbons," *Nature (London)*, vol. 444, 2006.

[102] Z. F. Wang and F. Liu, "Giant magnetoresistance in zigzag graphene nanoribbon," *Appl. Phys. Lett.*, vol. 99, p. 042110, 2011.

[103] C. Tao, L. Jiao, O. V. Yazyev, Y. Chen, J. Feng, X. Zhang, R. B. Capaz, J. M. Tour, A. Zettl, S. G. Louie, H. Dai, and M. F. Crommie, "Spatially resolving edge states of chiral graphene nanoribbons," *Nature Physics*, vol. 7, pp. 616–620, 2007.

[104] C. Dean, A. Young, L. Wang, I. Meric, G. Lee, K. Watanabe, T. Taniguchi, K. Shepard, P. Kim, and J. Hone, "Graphene based heterostructures," *Solid State Communications*, vol. 152(15), p. 12751282, 2012.

[105] G. Eda, T. Fujita, H. Yamaguchi, D. Voiry, M. Chen, and M. Chhowalla, "Coherent atomic and electronic heterostructures of single-layer mos2," *ACS Nano*, vol. 6 (8), p. 73117317, 2012.

[106] K. S. Novoselov and A. H. C. Neto, "Two-dimensional crystals-based heterostructures: materials with tailored properties," *Phys. Scr.*, vol. T146, p. 014006, 2012.

[107] B. Hunt, J. D. Sanchez-Yamagishi, A. F. Young, M. Yankowitz, B. J. LeRoy, K. Watanabe, T. Taniguchi, P. Moon, M. Koshino, P. Jarillo-Herrero, and R. C. Ashoori, "Massive dirac fermions and hofstadter butterfly in a van der waals heterostructure," *Science*, vol. 340, p. 1427, 2013.

[108] S. Bertolazzi, D. Krasnozhon, and A. Kis, "Nonvolatile memory cells based on mos2/graphene heterostructures," *ACS Nano*, vol. 7 (4), p. 32463252, 2013.

[109] S. B. Kumar, M. B. A. Jalil, and S. G. Tan, "High magnetoresistance in graphene nanoribbon heterojunction," *Appl. Phys. Lett.*, vol. 101, p. 183111, 2012.

[110] H. Yang, J. Heo, S. Park, H. J. Song, D. H. Seo, K.-E. Byun, P. Kim, I. Yoo, H.-J. Chung, and K. Kim, "Graphene barristor, a triode device with a gate-controlled schottky barrier," *Science*, vol. 336, no. 6085, pp. 1140–1143, 2012.

[111] A. K. Geim and I. V. Grigorieva, "Van der waals heterostructures," *Nature*, vol. 499, pp. 419 – 425, 2013.

[112] S. Chuang, R. Kapadia, H. Fang, T. C. Chang, W.-C. Yen, Y.-L. Chueh, and A. Javey, "Near-ideal electrical properties of InAs/WSe_2 van der Waals heterojunction diodes," *Appl. Phys. Lett.*, vol. 102, no. 24, JUN 17 2013.

[113] T. Georgiou, R. Jalil, B. D. Belle, L. Britnell, R. V. Gorbachev, S. V. Morozov, Y.-J. Kim, A. Gholinia, S. J. Haigh, O. Makarovsky, L. Eaves, L. A. Ponomarenko, A. K. Geim, K. S. Novoselov, and A. Mishcheno, "Vertical field-effect transistor based on graphene-WS_2 heterostructures for flexible and transparent electronics," *Nature Nanotechnology*, vol. 8, no. 2, pp. 100 – 103, 2012.

[114] W. J. Yu, Z. Li, H. Zhou, Y. Chen, Y. Wang, Y. Huang, and X. Duan, "Vertically stacked multi-heterostructures of layered materials for logic transistors and complementary inverters," *Nature Materials*, vol. 12, pp. 246 – 252, 2013.

[115] M. J. W. Rodwell, M. Le, and B. Brar, "Inp bipolar ics: Scaling roadmaps, frequency limits, manufacturable technologies," *Proc. IEEE*, vol. 96, no. 2, pp. 271 – 286, 2008.

[116] S. Datta, *Electronic Transport in Mesoscopic System*. Cambridge University Press, Cambridge, 1995.

[117] ——, *Quantum Transport Atom to Transistor*. Cambridge: Cambridge University Press, 2005.

[118] E. S. Morell, P. Vargas, L. Chico, and L. Brey, "Charge redistribution and interlayer coupling in twisted bilayer graphene under electric fields," *Phys. Rev. B*, vol. 84, p. 195421, 2011.

[119] R. E. Peierls, *Z. Phys.*, vol. 80, p. 763, 1933.

[120] N. A. Bruque, M. K. Ashraf, T. R. Helander, G. J. O. Beran, and R. K. Lake, "Conductance of a conjugated molecule with carbon nanotube contacts," *Phys. Rev. B*, vol. 80, no. 15, p. 155455, 2009. [Online]. Available: dx.doi.org/10.1103/PhysRevB.80.155455

[121] M. Galperin, S. Toledo, and A. Nitzan, "Numerical computation of tunneling fluxes," *J. Chem. Phys.*, vol. 117, pp. 10 817–10 826, 2002.

[122] Y. C. Huang, C. P. Chang, and L. M. F, "Magnetic and quantum confinement effects on electronic and optical properties of graphene ribbons," *Nanotechnology*, vol. 18, p. 495401, 2007.

[123] S. B. Kumar, M. B. A. Jalil, S. G. Tan, and G. Liang, "Magnetoresistive effect in graphene nanoribbon due to magnetic field induced band gap modulation," *J. Appl. Phys.*, vol. 108, p. 033709, 2010.

[124] ——, "The effect of magnetic field and disorders on the electronic transport in graphene nanoribbons," *J.Phys. Condens. Matter*, vol. 22, p. 375303, 2010.

[125] Ph.Avouris, Z.Chenand, and V.Perebeinos, *Nature Nanotechnology*, vol. 2, p. 605, 2007.

[126] U. Fano, "Effects of configuration interaction on intensities and phase shifts," *Phys. Rev.*, vol. 124, no. 6, pp. 1866 – 1878, 1961.